

## METALLICITY AND IONIZATION IN HIGH VELOCITY CLOUD COMPLEX C

JOSEPH A. COLLINS<sup>1</sup>, J. MICHAEL SHULL

University of Colorado, CASA, Department of Astrophysical & Planetary Sciences, Campus Box 389, Boulder, CO 80309  
jcollins@casa.colorado.edu, mshull@casa.colorado.edu

AND

MARK L. GIROUX

East Tennessee State University, Department of Physics, Astronomy, & Geology  
Box 70652, Johnson City, TN 37614  
girouxm@etsu.edu

*Draft version September 14, 2018*

### ABSTRACT

We analyze *HST* and *FUSE* ultraviolet spectroscopic data for eleven sight lines passing through the infalling high velocity cloud (HVC) Complex C. These sight lines pass through regions with H I column densities ranging from  $N_{\text{HI}} = 10^{18.1}$  to  $10^{20.1}$  cm<sup>-2</sup>. From [O I/H I] abundances, we find that Complex C metallicities range from 0.09 to 0.29  $Z_{\odot}$ , with a column density weighted mean of 0.13  $Z_{\odot}$ . Nitrogen (N I) is underabundant by factors of (0.01–0.07)(N/H)<sub>⊙</sub>, significantly less than oxygen relative to solar abundances. This pattern suggests nucleosynthetic enrichment by Type II SNe, consistent with an origin in the Galactic fountain or infalling gas produced in winds from Local Group galaxies. The range of metallicity and its possible ( $2\sigma$ ) dependence on  $N_{\text{HI}}$  could indicate some mixing of primordial material with enriched gas from the Milky Way, but the mixing mechanism is unclear. We also investigate the significant highly ionized component of Complex C, detected in C IV, Si IV, and O VI, but not in N V. High-ion column density ratios show little variance and are consistent with shock ionization or ionization at interfaces between Complex C and a hotter surrounding medium. Evidence for the former mechanism is seen in the Mrk 876 line profiles, where the offset in line centroids between low and high ions suggests a decelerating bowshock.

*Subject headings:* Galaxy: halo — ISM: clouds — ISM: abundances — quasars: absorption lines

### 1. INTRODUCTION

The origin of the objects known as high-velocity clouds (HVCs; Wakker & van Woerden 1997) remains a problem within the framework of Galaxy evolution. Traditionally studied through H I 21-cm emission, HVCs do not have a detectable stellar component, and they are characterized by line centroids, typically at negative local standard of rest velocities,  $V_{\text{LSR}}$ , that deviate from models of Galactic rotation. The subsolar metallicities of HVCs imply that some fraction of the gas consists of primordial material. The continuous infall of low-metallicity ( $\sim 0.1Z_{\odot}$ ) gas onto the disk is predicted by Galaxy formation models that seek to explain such phenomena as the G-dwarf problem (Pagel 1994). Although their distances are uncertain, HVCs may trace structure formation on Galactic or Local Group scales.

One of the best studied HVCs in recent years has been Complex C, infalling gas located at least 6 kpc distant (Wakker 2001). Consideration of its large angular size ( $\sim 2000$  deg<sup>2</sup>) effectively limits it to a nearby location in the Galactic halo. Complex C is pierced by more UV-bright quasar sight lines than any other high-velocity cloud, making it an ideal laboratory to investigate the nature of high-velocity gas. Ion abundances have been investigated in several studies (Wakker et al. 1999, Gibson et al. 2001, Richter et al. 2001, Collins et al. 2003 [hereafter CSG03], Tripp et al. 2003), all of which indicate that the complex has a subsolar metallicity. The most

robust of these studies utilize the [O I/H I] abundance<sup>2</sup> to determine metallicity. Since O I is coupled to H I through charge exchange, we can assume that [O I/H I]  $\approx$  (O/H). Other ion abundances such as [S II/H I] require substantial and uncertain ionization corrections to determine the elemental abundance. By investigating all Complex C *Far Ultraviolet Spectroscopic Explorer* (*FUSE*) and *Hubble Space Telescope* (*HST*) sight lines available at the time, CSG03 derived a metallicity range,  $Z = 0.1 - 0.25 Z_{\odot}$ , based on the three sight lines for which [O I/H I] could be measured.

This range of metallicities suggests that Complex C is a mixture of infalling primordial material (with  $Z \approx 0.1 Z_{\odot}$ ) and higher-metallicity material that is produced in the Galactic disk and then elevated in a “Galactic fountain” (Shapiro & Field 1976; Bregman 1980). Alternatively, such metal-poor gas might be expelled from Local Group dwarf galaxies into the Galactic halo. We hope to gain insight into how these two reservoirs entrain and mix by observing elemental abundances and ionization distributions in multiple sight lines through Complex C. Further evidence for an enrichment of Complex C by Galactic material comes from analysis of elemental abundances, whose pattern can yield information about the nucleosynthetic history of the constituent metals (Pettini 2004). Alpha-process elements (such as O,

<sup>2</sup> Throughout this work, for element  $X$ , this quantity is defined as,  $[X/H I] = \log\left(\frac{N(X)/N(HI)c}{A(X)_{\odot}}\right)$ , where  $A(X)_{\odot}$  is the solar abundance of element  $X$ . The solar abundances for several elements have changed considerably in the last few years (AGS05).

<sup>1</sup> Also at Front Range Community College, Larimer Campus, 4616 S. Shields St., Fort Collins, CO 80526

Si, and S) are produced predominantly by Type II supernovae (SNe), while Fe is produced primarily by Type Ia SNe. Nitrogen is produced mostly by lower mass stars in the asymptotic giant branch (AGB) stage. With the bulk of  $\alpha$ -element production occurring relatively soon after star-formation is initiated, the release of N and Fe into the ISM can lag S or O enrichment by  $\sim 250$  Myr (Henry et al. 2000). Many of the previous Complex C studies find that N is depleted significantly relative to the  $\alpha$ -elements, sometimes by as much as a factor of 10. Several studies also found evidence for a slight decrement in Fe that cannot be attributed to dust depletion. CSG03 suggest that this abundance pattern is consistent with enrichment by Type II SNe, followed by ejection from the star-forming region in a Galactic fountain before significant N and Fe enrichment.

If the infalling Complex C is mixing with fountain material, there should be observable signatures of that mixing. If mixing occurs more efficiently in the outer regions of the complex, while cloud cores remain relatively pristine, then one may expect to see an anti-correlation between component metallicity and  $N_{\text{HI}}$ . Based on the three sight lines with accurate [O I/H I] metallicities, CSG03 found evidence for such a dependence, with the highest column density sight line at the lowest metallicity. However, the statistics of the correlation are poor, and measurements of additional sight lines are needed.

Since the low ions track elemental abundances, Complex C is typically discussed in those terms. However, the cloud has multiphase structure consisting of highly ionized gas, detected in C IV, Si IV, and O VI (Fox et al. 2004; hereafter F04). In previous work (Collins, Shull, & Giroux 2004, 2005, hereafter CSG04 and CSG05). discussed the presence of multiphase gas, produced in bow shocks produced at the interfaces between infalling HVCs in the Galactic halo. The  $H\alpha$  emission measures of Complex C and other HVCs are consistent with photoionization by escaping radiation from OB associations in the disk (Bland-Hawthorn & Putman 2001). CSG03 found that the low-ion abundance pattern in Complex C is consistent with such an ionization source. Although photoionization can explain the production of neutral and singly-ionized species, it cannot simultaneously explain the highly ionized component. F04 analyzed high ion ratios for the PG 1259+593 sight line and found that they are consistent with the production of highly ionized gas at the interface of Complex C and a hotter surrounding medium. Since Complex C is a known halo object with abundant quasar sight lines, it provides a test case for studying the production of highly ionized gas in the general HVC population (Sembach et al. 2003). The understanding of the production of highly ionized high-velocity gas is of particular interest for the study of the unusual class of “highly ionized HVCs” (Sembach et al. 1999; Collins, Shull, & Giroux 2004, 2005, hereafter CSG04 and CSG05). We have suggested (CSG04, CSG05) that the majority of highly ionized HVCs represent low column density analogs to objects such as Complex C, whereas Nicastro et al. (2002, 2003) have proposed that they trace shock-heated filaments of the warm-hot intergalactic medium (WHIM) at large distances. Better characterization of the highly ionized component of Complex C may shed light on the nature of the highly ionized HVCs.

Since the publication of CSG03, several new Complex C data sets from *FUSE* and *HST* appeared. These new datasets fall into one of three categories: 1) new or additional *FUSE* data that have increased the effective exposure time, in some cases significantly; 2) new *HST*-STIS E140M, E230M, or G140M exposures; 3) Mrk 205, a Complex C sight line of low- $N_{\text{HI}}$  with high quality *FUSE* and *HST*-STIS E140M data neglected in previous Complex C studies. Among these new datasets are *FUSE* spectra for 7 Complex C sight lines, including *HST*-STIS data for 5 of these 7 sight lines. We couple these new data with previously presented Complex C data for the 8 sight lines from CSG03 and one (3C 351) from Tripp et al. (2003). We update all previous column densities and abundances, using recent solar abundances (AGS05) and revised absorption oscillator strengths (Morton 2003). With this sample, we investigate issues of Complex C metallicity, gas mixing, relative abundances, and high ion production. The *FUSE* and *HST* observations are reductions discussed in § 2. The results for the analysis for the new sight lines are presented in § 3. Finally, in § 4 we discuss and interpret the results.

## 2. DESCRIPTION OF OBSERVATIONS AND REDUCTIONS

The new Complex C sight line data for this investigation include *FUSE* and *HST*-STIS datasets that were either previously unanalyzed or taken since the work for CSG03 was completed. All datasets were obtained from the publicly available Multimission Archive (MAST) at the Space Telescope Science Institute. Of the eight sight lines from CSG03, five have new *FUSE* or *HST*-STIS datasets, including Mrk 279, Mrk 290, Mrk 501, Mrk 876, and PG 1626+554. Also included here are *FUSE* and *HST*-STIS data for the sight lines HS 1543+5921 and Mrk 205, previously unanalyzed in the context of Complex C. Table 1 summarizes the observations that have new or unanalyzed *FUSE* and *HST*-STIS data.

Seven Complex C sight lines have new *FUSE* data. For a complete description of the *FUSE* instrument and its operation see Moos et al. (2000) and Sahnou et al. (2000). All sight lines were observed through the  $30'' \times 30''$  LWRS aperture in time-tag mode, except for the new C037 dataset for PG 1626+554, which was observed through the  $4'' \times 20''$  MDRS aperture. Owing to the small aperture size of the MDRS data, the target is not present in the PG 1626+554 SiC data. Calibrated *FUSE* data were extracted using a pass through the CALFUSE version 2.4 reduction pipeline. In order to improve signal-to-noise for these data, we include both “day” and “night” photons in the final calibrated spectra. The inclusion of “day” photons leads to strong airglow contamination of interstellar O I and N I absorption lines. However, the contamination is generally centered at  $V_{LSR} = 0$  km s $^{-1}$  and does not affect the higher-velocity Complex C absorption. Individual exposures were coadded, weighted by their signal-to-noise, to yield a final spectrum. Before coadding datasets taken several years apart, we checked spectra for unusual differences between datasets. If the differences were judged to be severe, then offending datasets were not included in the final coadded spectrum. In several cases, significant deviations were discovered between datasets taken at different times. The most significant difference was a

TABLE 1  
SUMMARY OF NEWLY ANALYZED OBSERVATIONS<sup>a</sup>

Sightline	FUSE Program ID	FUSE $T_{\text{exp}}$ (ks) <sup>b</sup>	HST-STIS Grating	HST Program ID	HST-STIS $T_{\text{exp}}$ (ks)
HS 1543+5921	P108	8.5	G140M	9784	25.3, 54.0, 49.5 <sup>c</sup>
Mrk 205	Q106, S601, D054	203.6	E140M	8625	78.3
Mrk 279	P108, D154	181.8	E140M	9688	41.4
Mrk 290	D076, E084	68.1	E230M	8150	32.5
Mrk 501	P107, C081	31.7	...	...	...
Mrk 876	P107, D028	129.1	E140M	9754	29.2
PG 1626+554	P107, C037	98.5	...	...	...

<sup>a</sup>Including only sight lines that either have data yet to be published for a Complex C study or have additional data since publication of CSG03.

<sup>b</sup>Effective exposure time for the LiF1a channel.

<sup>c</sup>G140M observations are taken at three separate grating tilts. The three listed exposure times are for central wavelengths of 1222 Å, 1272 Å, and 1321 Å, respectively.

factor of  $\gtrsim 5$  decrease in the flux of Mrk 279 in its 2002 data. The 2002 data are not included in our final Mrk 279 spectrum. Other less significant differences warranting rejected data for specific LiF or SiC segments include the absence of segment data or a strong continuum deviation.

A single resolution element of the *FUSE* spectrum is about 20 km s<sup>-1</sup> ( $\sim 10$  pixels) and, as a result data are oversampled at that resolution. Thus, to further improve signal-to-noise, we rebinned the data over 5 pixels. To set the absolute wavelength scale, we compared the centroid of Galactic H I 21-cm emission and aligned it to various Galactic absorption lines in the *FUSE* bandpass, such as those of Si II ( $\lambda 1020.70$ ), O I ( $\lambda 1039.23$ ), Ar I ( $\lambda \lambda 1048.22, 1066.66$ ), Fe II ( $\lambda \lambda 1125.45, 1144.94$ ), N I ( $\lambda 1134.17$ ), and various H<sub>2</sub> Lyman bands. We estimate the absolute wavelength scale to be accurate to within  $\sim 10$  km s<sup>-1</sup>.

The new *HST*-STIS data consist of observations taken with the E140M, E230M, or G140M gratings. The E140M and E230M echelle modes provide for a resolution of 7 km s<sup>-1</sup> over 1150–1700 Å and 10 km s<sup>-1</sup> over 1850–2700 Å, respectively. The HS 1543+5921 dataset is taken with the first-order G140M grating, covering the wavelength range 1194–1348 Å at a resolution of  $\sim 25$  km s<sup>-1</sup>. Final spectra were obtained by coadding individual exposures, weighted by their signal to noise. In order to both improve signal-to-noise and to match pixel size in velocity to that of the rebinned *FUSE* data, we rebinned the E140M and E230M echelle data to 3 pixels, while no rebinning was used for the first-order G140M spectrum. Finally, we set the absolute wavelength scale as for the *FUSE* data, comparing the N I ( $\lambda 1199.550$ ) and S II ( $\lambda 1250.584, 1253.811, 1259.519$ ) lines to the centroid of Galactic H I emission.

### 3. MEASUREMENTS FROM NEW DATA

In this section, we present measurements of ion column densities from the new data for Complex C sight lines. In each of these sight lines, except Mrk 501, we detect metal-line absorption associated with Complex C. The Mrk 501 data exhibit features that are likely due to a low- $N_{\text{HI}}$  Complex C component, although the low signal to noise in that data prevents measurements greater than  $3\sigma$  significance for any of the Complex C features. As a result, the Mrk 501 sight line provides only weak upper

limits on abundances, and we do not discuss the sight line further.

In order to measure column densities of ion species, we begin by extracting individual line profiles from the full *FUSE* and *HST*-STIS spectra. These profiles are normalized by fitting low-order polynomials to the continuum  $\pm 3$ –10 Å about the line in question, although in a number of cases spurious features near the line required the use of a much larger region for continuum measurement. For each sight line, we determine the velocity range of Complex C from the H I profile. We then measure the equivalent width,  $W_\lambda$ , of an absorption feature by integrating the line over the velocity range occupied by Complex C. This technique works well for low ions (neutral or singly-ionized), but high-ions (C IV, Si IV, O VI) can extend in velocity by as much as 45 km s<sup>-1</sup> beyond the bounds established by the H I profile. In those cases, we integrate the high ions over the full observed high-velocity absorption. When lines cannot be measured, we estimate  $3\sigma$  upper limits to  $W_\lambda$ .

The *FUSE* bandpass contains numerous H<sub>2</sub> lines that often contaminate high-velocity absorption for metal lines. In cases of weak contamination of high-velocity features, we can often quantify the contribution from contaminating H<sub>2</sub>. In order to model the contribution from a contaminating H<sub>2</sub> line, we analyze other isolated H<sub>2</sub> lines of the same rotation state  $J$ . By fitting several lines for a given  $J$  with Gaussian profiles, and fitting measured values of  $W_\lambda$  with a curve of growth, we can model the expected profile of the contaminant line. If the contamination of the Complex C feature is weak, we can subtract the contaminating absorption to reveal the Complex C profile and measure its equivalent width. An example of such a fit is shown in Figure 1 to the O I  $\lambda 1039.230$  line for Mrk 290. As indicated by the H<sub>2</sub>-subtracted profile, the remaining O I feature resembles other Complex C absorption lines seen in that sight line (see Figure 5 for other Mrk 290 profiles). In many cases, the H<sub>2</sub> contamination is too strong to accurately analyze the underlying Complex C profile (note the H<sub>2</sub> contamination of high-velocity O I  $\lambda 1039.230$  in the Component 2 profile for Mrk 876 in Figure 6).

In order to determine the column densities of ion species, we attempt to fit the data with a curve of growth. This requires the measurement of minimally two lines for

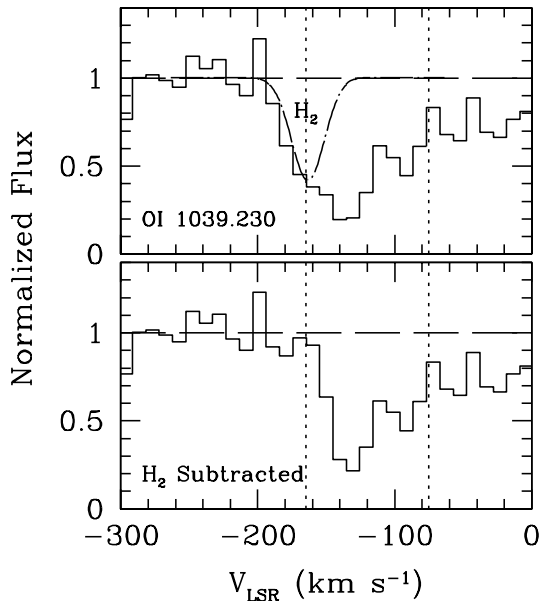


FIG. 1.— An example of the  $H_2$  fitting procedure to contaminated Complex C lines. Shown is the normalized profile of high-velocity absorption for the O I  $\lambda 1039.230$  line in the data of Mrk 290, along with the modeled profile of the Galactic L5-0 R(2)  $H_2$  line at 1038.69 Å (*top*). Also shown is the profile with the  $H_2$  model subtracted (*bottom*). The clean subtraction and the profiles similarity to those of other ions (as in Figure 5) indicates a successful subtraction. The vertical dashed lines indicate the  $-165$  to  $-75$   $\text{km s}^{-1}$  range of integration for Complex C as determined by the H I profile.

one species in any given Complex C component. We are able to empirically fit a curve of growth to low ions in Complex C components towards Mrk 205, Mrk 279, Mrk 290, and Mrk 876. In cases where a curve of growth cannot be fit, we use the apparent optical depth (AOD) method to measure column densities of lines that are clearly optically thin (Savage & Sembach 1991). In other cases, where unresolved saturation may be an issue, as occurs for the O I  $\lambda 1039.23$  line in particular, we estimate a range of possible column densities. Since the primary goal of this work is to specifically determine O I abundances, we estimate the column density range by using the observed spread in doppler  $b$ -values determined from curve-of-growth fits to data including O I lines in other Complex C sight lines. Considering all of the Complex C sight lines that we have analyzed here and in CSG03, the  $b$  values fitted to data that include O I lines range from  $10.2 \text{ km s}^{-1} \leq b \leq 18.0 \text{ km s}^{-1}$ . Using this spread of  $b$ -values, we can establish the range of possible column densities from lines of moderate optical depth. The high-ions C IV, Si IV, N V, and O VI probably reside in a different component than the low ions, and are thus not well described by a  $b$ -value determined from species of a lower degree of ionization. For the high-ions, we use the apparent optical depth method to measure column densities. All rest wavelengths and oscillator strengths are from Morton (2003).

Values of  $N_{\text{HI}}$  are measured from data taken at the Effelsberg 100-m telescope, except in the case of HS 1543+5921, for which we measure  $N_{\text{HI}}$  from data of the Leiden-Dwingeloo Survey (LDS; Hartmann & Bur-

TABLE 2  
SUMMARY OF MEASUREMENTS—HS 1543+5921 SIGHTLINE

Species	$\lambda^a$ (Å)	$f^a$	$W_\lambda^b$ (mÅ)	$\log N(X)^b$ ( $N$ in $\text{cm}^{-2}$ )
H I	...	...	...	$19.67^{+0.05}_{-0.07} (\pm 0.1)^c$
N I	1199.550	0.132	$151 \pm 24$	$[14.23^{+0.15}_{-0.14}, 14.92^{+0.49}_{-0.42}]$
N V	1238.821	0.156	$< 47$	$< 13.33$
S II	1259.518	0.0166	$42 \pm 9$	$14.30^{+0.08}_{-0.10}$
...	1253.805	0.0109	$27 \pm 9$	...

<sup>a</sup>Wavelengths and oscillator strengths from Morton (2003).

<sup>b</sup>Equivalent widths for Complex C integrated over velocity range  $-170$  to  $-105 \text{ km s}^{-1}$ . Error bars on measured column densities are  $1\sigma$ ; upper limits are  $3\sigma$ . Range of column densities for N I is calculated from curves of growth with doppler parameters,  $b = 10.2 \text{ km s}^{-1}$  and  $b = 18.0 \text{ km s}^{-1}$  (in brackets). All other lines use the AOD method, with S II column density based on 1259.518 Å line only.

<sup>c</sup>The  $N_{\text{HI}}$  column density includes a systematic error (in parentheses) of 0.1 dex because of the beam-size mismatch between H I 21-cm data and quasar absorption spectra.

ton 1997). We adopt the Effelsberg  $N_{\text{HI}}$  values quoted in Wakker et al. (2003), except in the cases of Mrk 279 and Mrk 876, which exhibit blended multi-component Complex C structure. In those cases, we directly integrate the Effelsberg profile to calculate  $N_{\text{HI}}$ . The beam sizes of the Effelsberg telescope and LDS are  $9'.1$  and  $36'$ , respectively, whereas the beam size in quasar absorption spectroscopy is effectively determined by the sub-arcsecond angular size of the quasar emitting region. Therefore, the measured values sample column densities on a much larger scale than the metal ion column densities. Wakker et al. (2001) compare  $N_{\text{HI}}$  for targets measured through both  $\text{Ly}\alpha$  absorption in *HST* data with H I emission in Effelsberg data. They find that  $N_{\text{HI}}$  varies by as much as 25% between these two techniques. We therefore adopt a systematic error for  $N_{\text{HI}}$  measurements of 0.1 dex. This uncertainty becomes relevant when we determine ion abundances in § 4.

### 3.1. HS 1543+5921

HS 1543+5921 is an extragalactic target that was observed with the *HST*-STIS G140M grating for a program investigating an intervening low-surface-brightness galaxy (Bowen et al. 2005). The target has a low UV flux ( $\sim 2 \times 10^{-15} \text{ ergs s}^{-1} \text{ cm}^{-2} \text{ \AA}^{-1}$ ) and long exposures were taken at three different grating tilts covering the wavelength range 1194–1348 Å. A short 8 ks *FUSE* exposure exists for this sight line, but due to the low flux of the target, those data are of insufficient quality for absorption line studies.

Several of the prominent absorption lines observed in the available STIS bandpass are shown in Figure 2 along with the LDS profile of H I emission. The H I profile shows a prominent Complex C component that we measure at  $\log N(\text{H I}) = 19.66^{+0.03}_{-0.05}$  from direct integration of the LDS profile. Based on the observed line profiles, we adopt a Complex C integration range of  $-170 < V_{\text{LSR}} < -105 \text{ km s}^{-1}$ . The Complex C component is easily detected in N I  $\lambda 1199.55$ , Si III  $\lambda 1206.50$ , S II  $\lambda\lambda 1253.81, 1259.52$ , O I  $\lambda 1302.17$ , and Si II  $\lambda 1260.42$ . Owing to saturation and blending

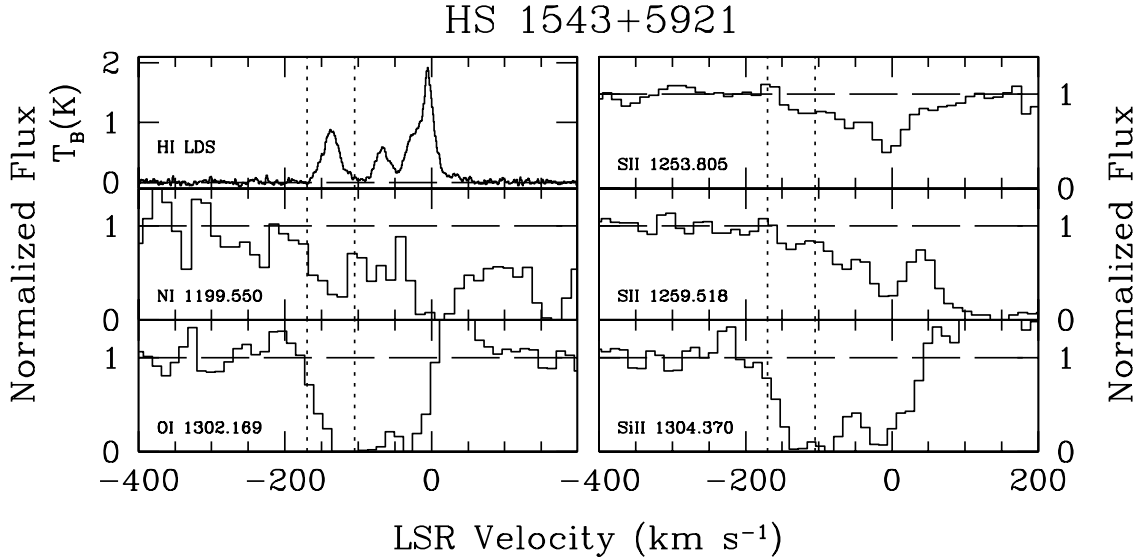


FIG. 2.— A sample of normalized absorption profiles from *HST* STIS G140M data for HS 1543+5921, along with the LDS profile of H I emission. The vertical dashed lines indicate the  $-170$  to  $-105$   $\text{km s}^{-1}$  range of integration for measurements of  $W_\lambda$ .

with a strong intermediate-velocity component, we are unable to properly measure column densities of O I and Si II based on the profiles for O I  $\lambda 1302$  and Si II  $\lambda 1304$  presented in Figure 2. Only the S II and N I lines are sufficiently distinguishable from lower velocity absorption for equivalent width and column density measurements. Equivalent widths of measured species are shown in Table 2.

Although we have measurements for two S II lines, they provide no constraint on the doppler parameter since they are both clearly optically thin lines. Since there are insufficient absorption lines for a good curve-of-growth analysis, we utilize the AOD method for determining column densities in cases where the profiles are clearly optically thin. AOD measurements of the S II lines give values of  $\log N(\text{S II})$  that are within 0.01 dex of one another. We adopt the measurement from the 1259.52 Å line, based on its cleaner and deeper profile. The N I  $\lambda 1199.55$  Complex C feature is quite strong, and unresolved saturation may be an issue. For that line, we establish a range of possible N I column densities based on the range of observed O I-based  $b$  values ( $10.2 \text{ km s}^{-1} < b < 18.0 \text{ km s}^{-1}$ ) from our full Complex C sight line sample. Measured column densities are reported in Table 2. Owing to the strength of the N I 1199.55 line in Complex C, the range of possible N I column densities extends over a factor of 5. This low end of the range represents the nearly optically thin case, while the upper end of the range represents the highest level of saturation seen in similar strength lines in our Complex C sample.

### 3.2. Mrk 205

The Mrk 205 sight line passes through a thin, yet detectable, H I column of Complex C. From Effelsberg H I data, Wakker et al. (2003) report a value of  $N(\text{H I}) = (1.3 \pm 0.3) \times 10^{18} \text{ cm}^{-2}$  for the Complex C component in this sight line, the lowest  $N_{\text{HI}}$  of the Complex C regions in this study. Owing in part to its low column density, this sight line has yet to be investigated

thoroughly in previous Complex C studies.

There are currently 204 ks of *FUSE* data available and a long 78 ks *HST*-STIS E140M exposure for Mrk 205. Because of the low Complex C column density in this sight line, this component cannot be detected in lines of O I, Si II, or Fe II with *FUSE*, since lines of those species in the *FUSE* bandpass are relatively weak compared to their counterparts in the STIS E140M bandpass. The only low-ion absorption line in the *FUSE* bandpass for which the Complex-C component is detected is in the strong C II  $\lambda 1036.34$  line. The Complex-C component is clearly detected in several absorption lines in the STIS E140M bandpass, including the crucial O I  $\lambda 1302.17$  line. Several of the observed line profiles are shown in Figure 3, along with the LDS profile of H I emission. The LDS profile shows weak Complex-C emission at  $V_{\text{LSR}} = -145 \text{ km s}^{-1}$ , along with strong H I emission at  $V_{\text{LSR}} \approx 200 \text{ km s}^{-1}$ , from a compact high-velocity cloud labeled WW84 (Wakker et al. 2003) that is unrelated to Complex C. Based on the observed absorption features in this sight line, we adopt an integration range of  $-165 < V_{\text{LSR}} < -125 \text{ km s}^{-1}$  for the Complex-C component. Measured equivalent widths are shown in Table 3.

The Complex C component is detected in three Si II and two C II lines. We have fitted a curve of growth to those lines with doppler parameter  $b = 7.0_{-1.1}^{+1.8} \text{ km s}^{-1}$ . The resulting column densities are presented in Table 3. Such a low doppler parameter suggests some amount of unresolved saturation in the profiles. Because this curve of growth is based on only a few lines, we hold some concern for its accuracy when applied to other absorption lines beyond those of Si II and C II, despite the small error bars on the doppler parameter. Since the O I line is relatively weak, the choice of doppler parameter has little influence on the resulting O I column density. In fact, the value of  $N(\text{O I})$  calculated from the curve of growth differs from the value calculated with the AOD

TABLE 3  
SUMMARY OF MEASUREMENTS—MRK 205 SIGHTLINE

Species	$\lambda^a$ (Å)	$f^a$	$W_\lambda^b$ (mÅ)	$\log N(X)^b$ ( $N$ in $\text{cm}^{-2}$ )
H I	...	...	...	$18.11^{+0.09}_{-0.11}(\pm 0.1)^c$
C II	1036.337	0.118	$70 \pm 6$	$14.48^{+0.15}_{-0.30}$
...	1334.532	0.128	$106 \pm 3$	...
C IV	1548.204	0.190	$< 25$	$< 12.84$
N I	1199.550	0.132	$< 25$	$< 13.26$
N V	1238.821	0.156	$< 16$	$< 12.85$
O I	1302.169	0.0480	$47 \pm 3$	$13.99^{+0.06}_{-0.06}$
O VI	1031.926	0.133	$< 22$	$< 13.25$
Al II	1670.787	1.740	$22 \pm 6$	$11.77^{+0.12}_{-0.16}$
Si II	1193.290	0.582	$50 \pm 12$	$13.11^{+0.13}_{-0.09}$
...	1260.422	1.18	$78 \pm 4$	...
...	1304.370	0.0863	$16 \pm 3$	...
Si III	1206.500	1.63	$> 113$	$> 13.00$
Si IV	1393.760	0.513	$< 23$	$< 12.42$
S II	1259.518	0.0166	$< 14$	$< 13.82$
Ar I	1048.220	0.263	$< 17$	$< 12.89$
Fe II	1608.451	0.0577	$< 30$	$< 13.43$

<sup>a</sup>Wavelengths and oscillator strengths from Morton (2003).

<sup>b</sup>Equivalent widths for Complex C integrated over velocity range  $-165$  to  $-125$   $\text{km s}^{-1}$ . Error bars on measured column densities are  $1\sigma$ ; upper limits are  $3\sigma$ . Column densities are calculated from curve of growth with doppler parameter,  $b = 7.0^{+1.8}_{-1.1}$   $\text{km s}^{-1}$ , except O VI, N V, C IV, Si IV, and Si III where we used the AOD method.

<sup>c</sup>The  $N_{\text{HI}}$  column density includes a systematic error (in parentheses) of 0.1 dex due to beam-size mismatch between H I 21-cm data and quasar absorption spectra.

method by only 0.07 dex.

We note that the Complex C component is not detected in any of the ions ionized beyond Si III. Since the C IV absorption feature near the Complex C integration range bears little resemblance to other Complex C features, we suspect it may be spurious absorption and unrelated to Complex C. Limits on the column densities of the high ions are presented in Table 3. For sight lines that have easily detectable low ions, this is the only Complex C sight line where associated O VI is not detected.

### 3.3. Mrk 279

Since CSG03, 137 ks of additional *FUSE* data have been taken for this sight line, and extensive *HST*-STIS E140M exposures have recently been obtained. The *FUSE* and *HST* spectra were observed simultaneously in both 2002 and 2003. The 2002 spectra indicate that the quasar flux is lower by at least a factor of 5 than the original 1999/2000 *FUSE* exposure and the 2003 spectra. We therefore do not include the 2002 data in our final Mrk 279 spectrum.

The Mrk 279 *FUSE* and STIS data have the highest signal to noise among the Complex C sight lines. Samples of the analyzed line profiles are shown in Figure 4, along with the Effelsberg profile of H I emission. The component structure along this sight line is complicated; Wakker et al. (2003) identified eight components to the H I profile, two of which are attributed to Complex C. CSG03 adopted the approach of integrating over both HVC components, even though contamination from higher-metallicity components at lower velocity was

TABLE 4  
SUMMARY OF MEASUREMENTS—MRK 279 SIGHTLINE

Species	$\lambda^a$ (Å)	$f^a$	$W_\lambda^b$ (mÅ)	$\log N(X)^b$ ( $N$ in $\text{cm}^{-2}$ )
H I	...	...	...	$19.27^{+0.08}_{-0.11}(\pm 0.1)^c$
C IV	1548.204	0.190	$73 \pm 6$	$13.30^{+0.04}_{-0.04}$
N I	1199.550	0.132	$26 \pm 6$	$13.22^{+0.10}_{-0.12}$
N II	1083.994	0.111	$150 \pm 7$	$14.45^{+0.11}_{-0.10}$
N V	1238.821	0.156	$< 14$	$< 12.84$
O I	929.517	0.00229	$19 \pm 6$	$14.98^{+0.10}_{-0.06}$
...	936.630	0.00365	$28 \pm 6$	...
...	948.686	0.00631	$41 \pm 7$	...
...	971.738	0.0116	$75 \pm 6$	...
...	976.448	0.00331	$24 \pm 6$	...
...	1039.230	0.00907	$68 \pm 3$	...
...	1302.169	0.0480	$208 \pm 4$	...
O VI	1031.926	0.133	$52 \pm 4$	$13.66^{+0.04}_{-0.04}$
Al II	1670.787	1.740	$208 \pm 9$	$12.96^{+0.09}_{-0.07}$
Si II	1020.699	0.0168	$22 \pm 4$	$14.14^{+0.06}_{-0.08}$
...	1190.416	0.292	$198 \pm 6$	...
...	1193.290	0.582	$244 \pm 6$	...
...	1304.370	0.0863	$114 \pm 4$	...
...	1526.707	0.133	$183 \pm 6$	...
Si IV	1393.760	0.513	$45 \pm 6$	$12.73^{+0.05}_{-0.05}$
P II	963.801	1.460	$< 17$	$< 12.18$
S II	1259.518	0.0166	$11 \pm 3$	$13.69^{+0.11}_{-0.15}$
Ar I	1048.220	0.263	$< 12$	$< 12.69$
Fe II	1096.877	0.0327	$22 \pm 4$	$13.85^{+0.11}_{-0.10}$
...	1121.975	0.0290	$17 \pm 4$	...
...	1125.448	0.0156	$15 \pm 5$	...
...	1144.938	0.0830	$55 \pm 5$	...
...	1608.451	0.0577	$80 \pm 6$	...

<sup>a</sup>Wavelengths and oscillator strengths from Morton (2003).

<sup>b</sup>Equivalent widths for Complex C are integrated over velocity range  $-200$  to  $-120$   $\text{km s}^{-1}$ . Error bars on measured column densities are  $1\sigma$ ; upper limits are  $3\sigma$ . Column densities are calculated from curve of growth with doppler parameter,  $b = 18.0^{+2.0}_{-1.5}$   $\text{km s}^{-1}$ , except for O VI, N V, C IV, and Si IV, where we used AOD method.

<sup>c</sup>The  $N_{\text{HI}}$  column density includes a systematic error (in parentheses) of 0.1 dex because of beam-size mismatch between H I 21-cm data and quasar absorption spectra.

a possibility. Here, we take the approach of integrating over only the highest-velocity Complex C component,  $-200 < V_{\text{LSR}} < -120$   $\text{km s}^{-1}$ , so as to be reasonably sure that no contamination from non-Complex C absorption occurs. The high-ions, particularly C IV and O VI, extend more blueward than the lower ions. Therefore, we extend the integration range for measurements of the highly ionized component out to  $V_{\text{LSR}} = -215$   $\text{km s}^{-1}$ . The weaker lines of the C IV and Si IV doublets were not detected, whereas the stronger lines (C IV  $\lambda 1548$  and Si IV  $\lambda 1393$ ) were seen at optical depths  $\tau \approx 0.2$  in 7  $\text{km s}^{-1}$  resolution bins. We believe the weaker lines were on the margin of detectability (at  $\sim 2\sigma$  level) at  $S/N \approx 19 - 26$  per resolution element.

Equivalent widths for measurements of the highest-velocity Complex C component are shown in Table 4. We have detected the Complex C component in seven O I, five Si II, and five Fe II lines. From the equivalent width measurements of these lines, we have determined a best fit curve of growth with doppler parameter,  $b = 18.0^{+2.0}_{-1.5}$   $\text{km s}^{-1}$ . Resulting column densities of the various ion

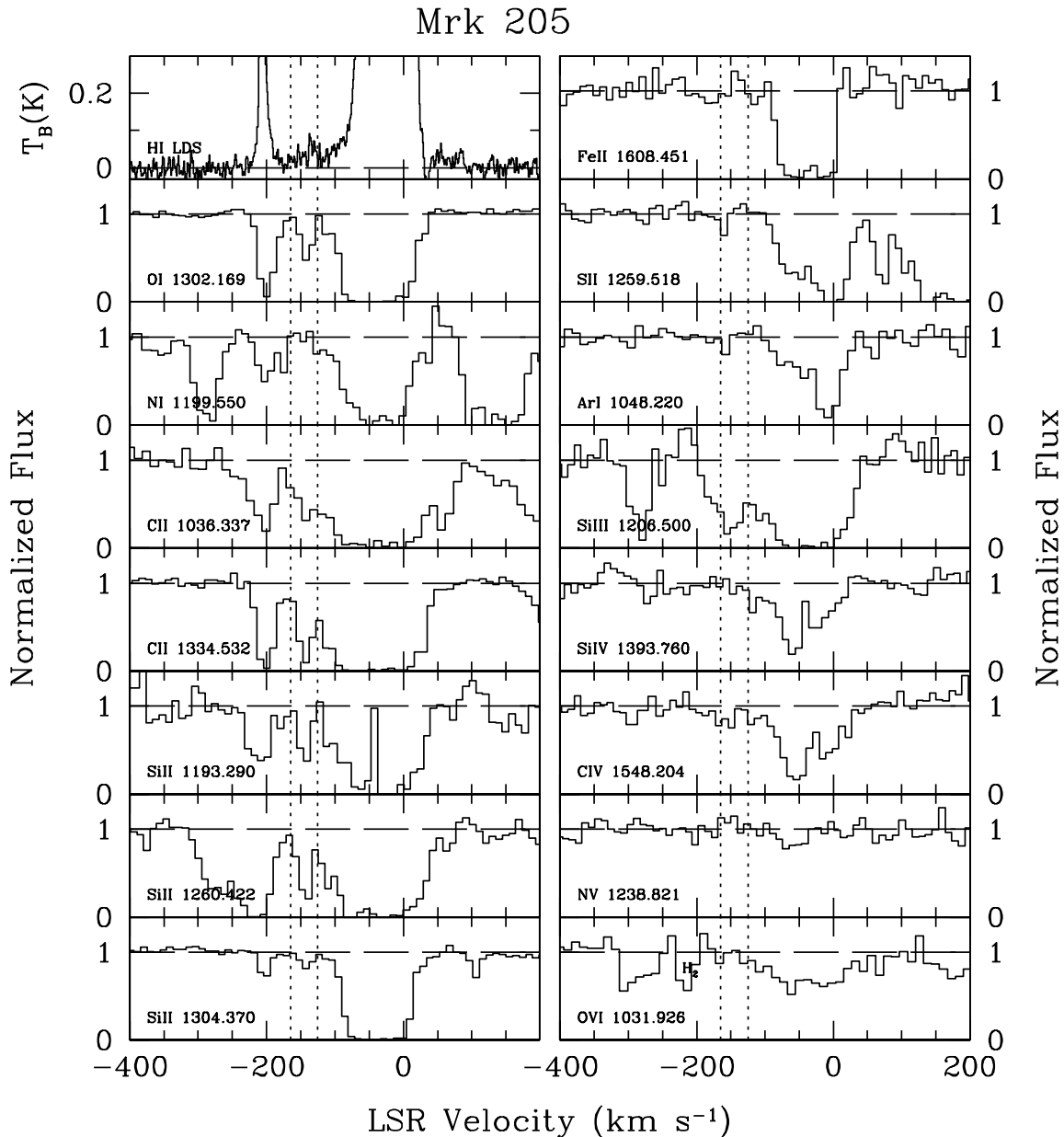


FIG. 3.— A sample of normalized absorption profiles from *FUSE* and *HST* STIS E140M data for Mrk 205, along with the LDS profile of H I emission. The vertical dashed lines indicate the  $-165$  to  $-125$   $\text{km s}^{-1}$  range of integration for measurements of  $W_\lambda$ .

species are shown in Table 4. The H I column density was determined by direct integration of the Effelsberg profile over the specified velocity range.

#### 3.4. Mrk 290

The Mrk 290 sight line was the first Complex C target investigated with UV spectra. Using Goddard High-Resolution Spectrograph (GHRS) data for Mrk 290, Wakker et al. (1999) determined a Complex C metallicity of  $0.1 Z_\odot$  based on the S II/H I abundance. The CSG03 analysis used a brief *FUSE* exposure to measure upper limits on ion abundances. Since CSG03, a substantial *FUSE* exposure has been obtained to supplement the previously available GHRS data. In addition, an archival STIS E230M dataset is available, which covers strong

Fe II lines in the  $2300$ – $2600$   $\text{\AA}$  range.

Figure 5 shows a sample of the analyzed line profiles, along with the LDS profile of H I emission. Based on the various line profiles, we adopt an integration range of  $-165 < V_{LSR} < -75$   $\text{km s}^{-1}$ , except for O VI which extends blueward to  $-210$   $\text{km s}^{-1}$ . We see evidence for a two-component structure in the Complex C absorption for several absorption lines, most notably the Fe II lines in the higher signal-to-noise STIS data. However, the primary goal of this work is to determine O I abundances using a technique that relies heavily on weaker O I lines in the SiC channels. The SiC data for Mrk 290 have low signal to noise, and multi-component structure is not apparent for most O I lines, although high-velocity absorption is clearly present. As a result, we consider

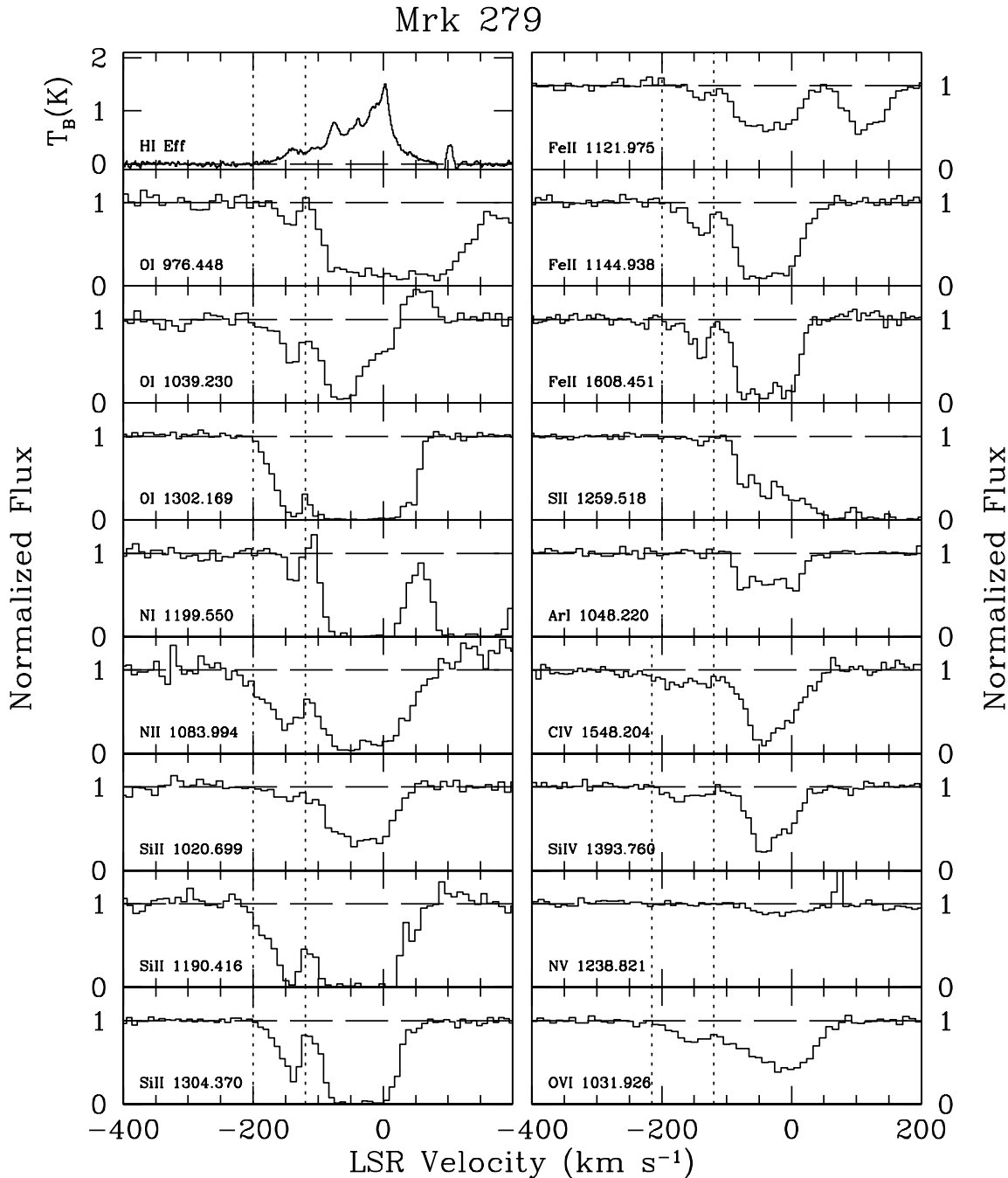


FIG. 4.— A sample of normalized absorption profiles from *FUSE* and *HST* STIS E140M data for Mrk 279, along with the Effelsberg profile of H I emission. The vertical dashed lines indicate the  $-200$  to  $-120$   $\text{km s}^{-1}$  range of integration for measurements of  $W_\lambda$ , except for the high ions, C IV, Si IV, N V, and O VI, where measurements extend to as low as  $-215$   $\text{km s}^{-1}$ .

the entire Complex C velocity range as a single feature. Because  $\text{H}_2$  contamination is a problem for several Complex C absorption features in the *FUSE* bandpass, we have modeled the expected profiles of contaminant  $\text{H}_2$  lines, shown also in Figure 5.

Equivalent width measurements of Complex C absorption in this sight line are shown in Table 5. We also include S II  $\lambda 1259.518$  and N V  $\lambda 1238.821$  results from the GHRs data. Using results from the 6 O I and 7 Fe II line measurements, we determine a best-fit curve of growth with doppler parameter,  $b = 13.4_{-2.9}^{+4.3}$   $\text{km s}^{-1}$ .

Resulting column densities are listed in Table 5.

### 3.5. Mrk 876

The Complex C Mrk 876 sight line was investigated both by Murphy et al. (2000) and CSG03. These studies were unable to make measurements of O I owing to strong  $\text{H}_2$  contamination and poor data quality in the SiC channels. Since those publications, 80 ks of additional *FUSE* data and a high-quality *HST*-STIS E140M dataset have become available.

A sample of the analyzed line profiles are shown in



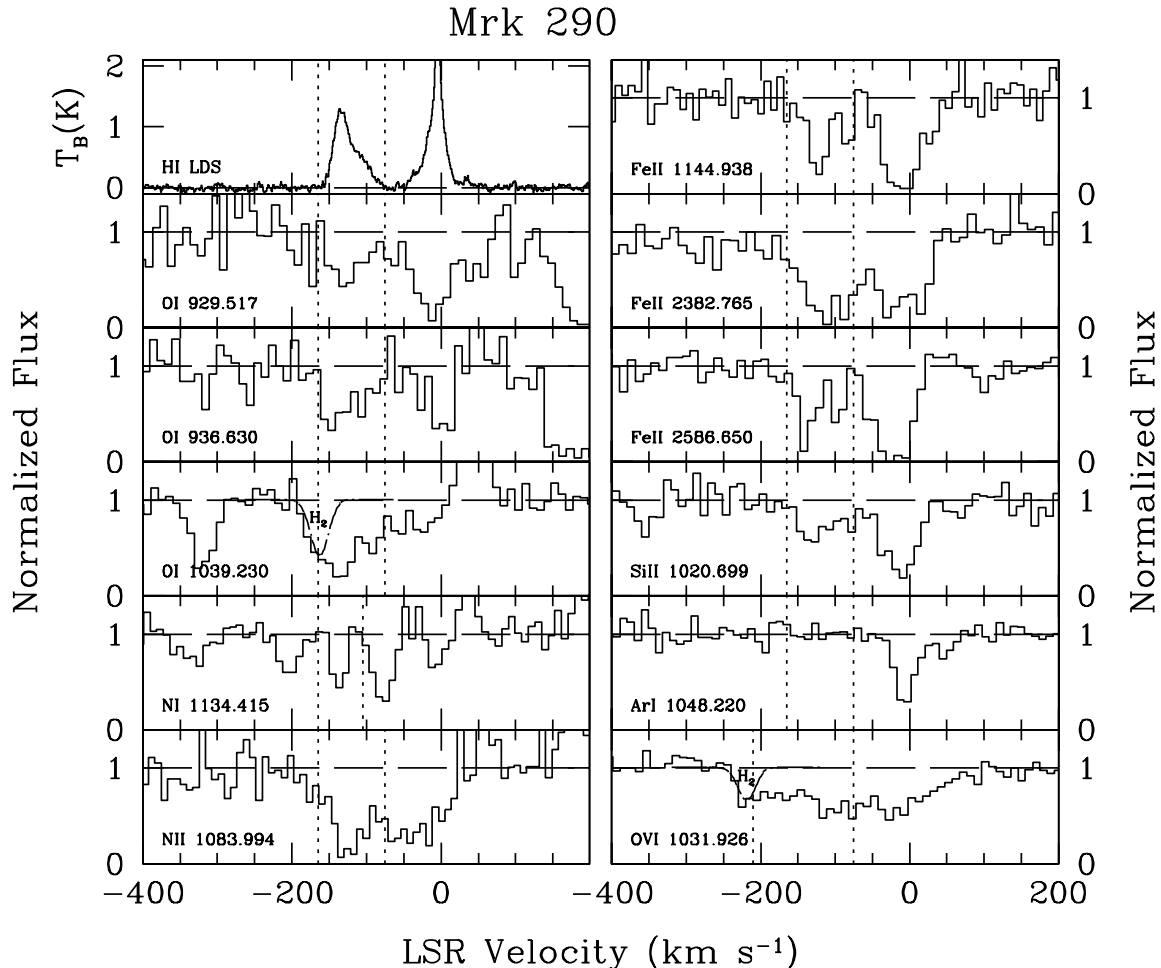


FIG. 5.— A sample of normalized absorption profiles from *FUSE* and *HST* STIS E230M data for Mrk 290, along with the LDS profile of H I emission. The vertical dashed lines indicate the  $-165$  to  $-75$   $\text{km s}^{-1}$  range of integration for measurements of  $W_\lambda$ , except for O VI, where measurements extend to a minimum velocity of  $-210$   $\text{km s}^{-1}$ . The O I and O VI profiles include a fit to  $\text{H}_2$  contamination.

Figure 6, along with the Effelsberg profile of H I emission. Both the H I analysis by Wakker et al. (2003) and the line profiles presented here indicate a two-component structure for Complex C in this direction. Based on these profiles, we adopt integration ranges of  $-155 < V_{LSR} < -85$   $\text{km s}^{-1}$  and  $-210 < V_{LSR} < -155$   $\text{km s}^{-1}$ , which we identify as Component 1 (centered at  $V_{LSR} \approx -135$   $\text{km s}^{-1}$ ) and Component 2 (centered at  $V_{LSR} \approx -175$   $\text{km s}^{-1}$ ), respectively. This sight line pierces a particularly thick column of Galactic  $\text{H}_2$ ,  $N(\text{H}_2) \approx 4.4 \times 10^{16}$   $\text{cm}^{-2}$  (Gillmon et al. 2006). Fits to contaminant  $\text{H}_2$  lines are shown in several of the profiles.

Table 6 shows equivalent width measurements for Components 1 and 2 of lines in the *FUSE* and *HST*-STIS E140M bandpass. Multiple lines of O I, Si II, and Fe II are detected for each component. To those measurements, we fitted curves of growth to Components 1 and 2 of  $b = 17.8^{+2.0}_{-1.8}$   $\text{km s}^{-1}$  and  $b = 15.4^{+3.5}_{-2.5}$   $\text{km s}^{-1}$ , respectively. Table 6 also shows the resulting column densities calculated from the curves of growth. We calculate  $N_{\text{HI}}$  for each component by direct integration of the Effelsberg H I profile.

The high ions C IV and Si IV show an unusual velocity structure, which is offset to lower velocities from the

low ions. The high-ion profiles show peak absorption at  $V_{LSR} \approx -95$   $\text{km s}^{-1}$ , well redward of the low ions. Additionally, we detect little evidence of the two-component structure seen in the low ions, except possibly in the case of C IV  $\lambda 1550.781$ . We adopt an integration range for the high-ions of  $-210 < V_{LSR} < -75$   $\text{km s}^{-1}$  and analyze those lines separately from Components 1 and 2. High-ion column densities of this component, calculated with the apparent optical depth method, are listed in Table 7.

### 3.6. PG 1626+554

At the time of publication of CSG03, only 8 ks of *FUSE* data were available for this sight line. An additional 90 ks of data were recently taken using the MDRS slit. Although the target is not present in the new SiC data, the current dataset does allow measurement of the strongest absorption lines in the 1000-1150 Å range.

Several of the observed line profiles are shown in Figure 7, along with the LDS profile of H I emission. We are able to make  $> 3\sigma$  measurements for only four absorption lines, including O I  $\lambda 1039.230$ , O VI  $\lambda 1031.926$ , Si II  $\lambda 1020.699$ , and Fe II  $\lambda 1144.938$ . Based on these profiles, we adopt an integration range of  $-155 < V_{LSR} < -75$   $\text{km s}^{-1}$ , except for the case of O VI, which appears to extend to larger negative velocity. The feature centered at

## Mrk 876

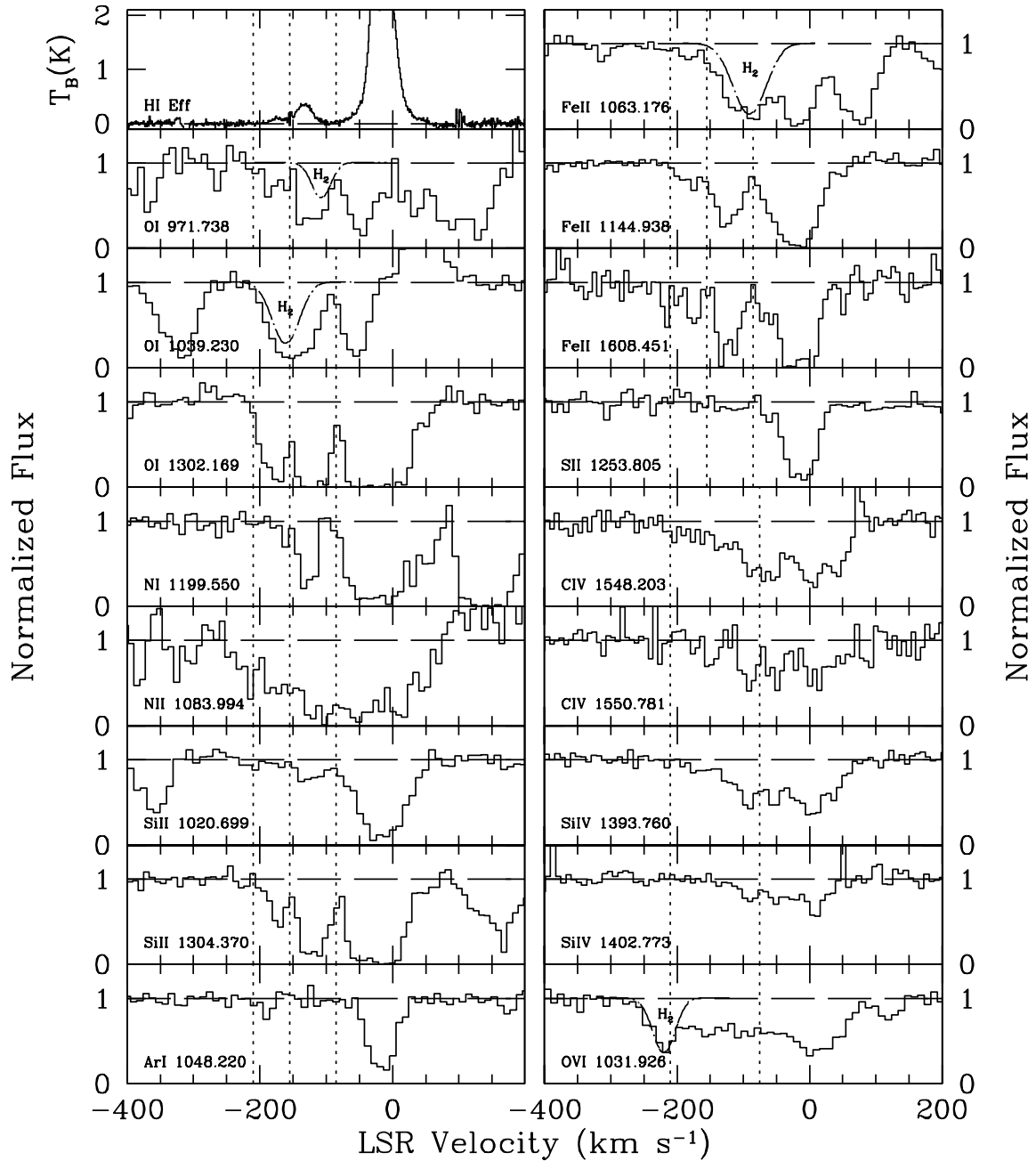


FIG. 6.— A sample of normalized absorption profiles from *FUSE* and *HST* STIS E140M data for Mrk 876, along with the Effelsberg profile of H I emission. The vertical dashed lines indicate the  $-155$  to  $-85$   $\text{km s}^{-1}$  and  $-210$  to  $-155$   $\text{km s}^{-1}$  ranges of integration for profiles where we make measurements of  $W_\lambda$  for Components 1 and 2 of Complex C. For the high ions, C IV, Si IV, N V, and O VI, our measurements are made over the range  $-210$  to  $-75$   $\text{km s}^{-1}$ . Also included are fits to contaminating  $\text{H}_2$  absorption.

$V_{LSR} \approx -215$   $\text{km s}^{-1}$  in the O VI profile is Lyman (6-0) [L6-0] P(3)  $\text{H}_2$  absorption. Owing to low signal to noise, the  $J = 3$   $\text{H}_2$  profiles in this dataset are sufficiently weak that we are unable to model an expected profile of the contamination in the O VI profile. Based on absorption due to the stronger L4-0 R(3) line, we can establish with certainty that the absorption in the O VI profile is uncontaminated by  $\text{H}_2$  redward of  $V_{LSR} = -180$   $\text{km s}^{-1}$ , and that absorption can be attributed to O VI. Thus, Complex C O VI in this sight line extends beyond low-ion

absorption, and we integrate over  $-180 < V_{LSR} < -75$   $\text{km s}^{-1}$  for its measurement.

Complex C equivalent width measurements for this sight line are shown in Table 8. Because of the limited number of line measurements, we are unable to empirically derive a curve-of-growth. Previous analysis suggested that saturation can be an issue with the O I  $\lambda 1039.230$  and Fe II  $\lambda 1144.938$  lines, and some saturation may be indicated by their profiles in Figure 7. Therefore, the apparent optical depth method may not accu-

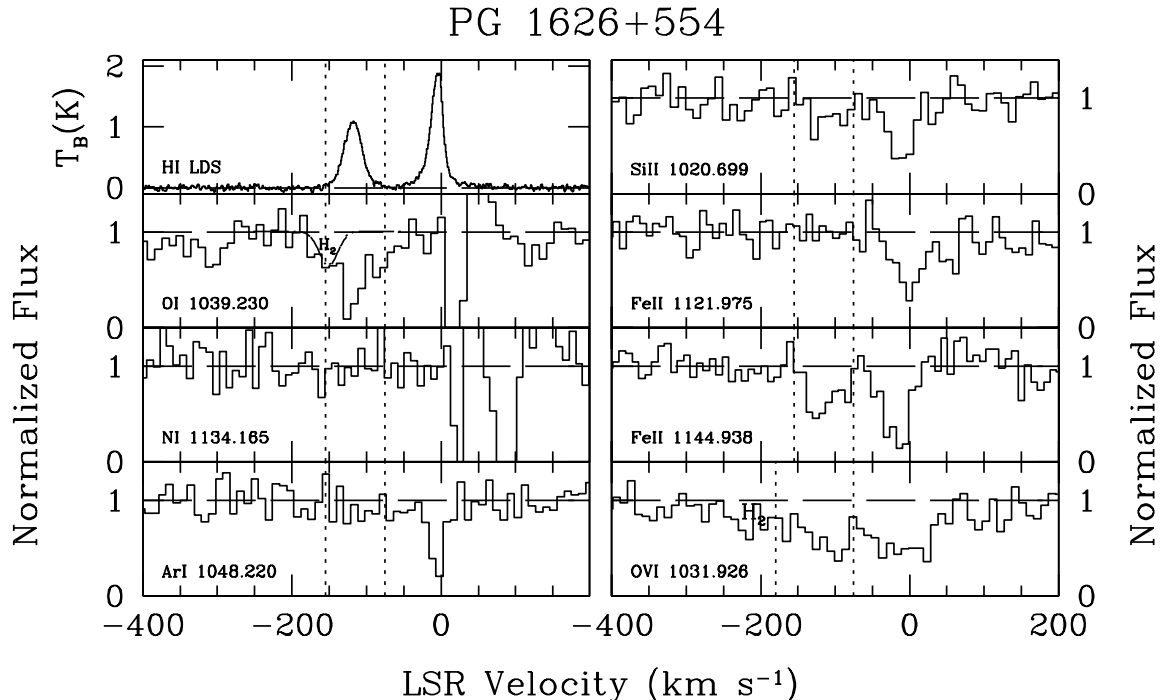


FIG. 7.— A sample of normalized absorption profiles from *FUSE* data for PG 1626+554, along with the LDS profile of H I emission. The vertical dashed lines indicate the  $-155$  to  $-75$   $\text{km s}^{-1}$  range of integration for measurements of  $W_\lambda$ , except for O VI, where measurements extend to a minimum velocity of  $-180$   $\text{km s}^{-1}$ . The O I profile includes a fit to  $\text{H}_2$  contamination.

rately determine O I and Fe II column density. We determine their range of possible column densities by considering the range of doppler parameters  $10.2 \leq b \leq 18.0$   $\text{km s}^{-1}$  for curve-of-growth fits to O I and Fe II lines in other Complex C sight lines. These column density ranges are shown in brackets in Table 8. All other column densities are calculated by the apparent optical depth method, including those from Si II  $\lambda 1020.70$  and O VI  $\lambda 1031.926$ , which are clearly optically thin lines.

#### 4. DISCUSSION

##### 4.1. Revised Solar Abundances and Atomic Data

With the measured column densities for the Complex C sight lines, we are now able to measure abundances, relative to the recently revised solar (photospheric) abundances (Asplund, Grevesse, & Sauval 2005, hereafter AGS05). In CSG03, we used solar abundances from Grevesse & Sauval (1998). The largest changes in our current analysis are:  $(\text{Ar}/\text{H})_\odot = 10^{-5.82}$ ;  $(\text{N}/\text{H})_\odot = 10^{-4.22}$ ; and  $(\text{O}/\text{H})_\odot = 10^{-3.34}$ . Substantial changes occurred for argon ( $\Delta A_{\text{Ar}} = -0.22$  dex), oxygen ( $\Delta A_{\text{O}} = -0.17$  dex), and nitrogen ( $\Delta A_{\text{N}} = -0.14$  dex). The abundances changed less significantly for silicon ( $\Delta A_{\text{Si}} = -0.04$  dex), sulfur ( $\Delta A_{\text{S}} = -0.06$  dex), and iron ( $\Delta A_{\text{Fe}} = -0.05$  dex).

Most of these abundances are only accurate to  $\pm 0.05$  (dex). However, the downward revisions in solar CNO abundances and of Ar, which is tied indirectly to oxygen, remain controversial. The revisions arise primarily from the application of time-dependent, non-LTE, 3D hydrodynamical models of the solar atmosphere, which have decreased the metal abundance in the solar convection zone by almost a factor of two, compared to pre-

vious compilations (Anders & Grevesse 1989; Grevesse & Sauval 1998). For example, the new solar abundances by mass of hydrogen, helium, and metals have  $X = 0.7392$ ,  $Y = 0.2486$ , and  $Z = 0.0122$  (AGS05), and thus have much lower  $Z/X = 0.0165$  compared to the previously recommended value of  $Z/X = 0.0275$  (Anders & Grevesse 1989). These lower metallicities are in poor agreement with helioseismological solar profiles of sound speed and density (Bahcall et al. 2005). They also disagree with C and O abundances derived from solar CO modeling. From their CO models, Ayres, Plymate, & Keller (2006) recommend a higher oxygen abundance,  $(7 \pm 1) \times 10^{-4}$ , a factor of 0.185 dex larger than that recommended by AGS05. We mention these issues, because it is possible that the reference solar abundance may change yet again. Therefore, one must regard the [O/H] metallicities in Complex C as relative values, which could drop by 0.10–0.15 dex if the standard solar oxygen abundance increases to accommodate the constraints from helioseismological data.

Additional small changes in metal-ion column densities arise from new curves of growth based on updated oscillator strengths for selected lines (Morton 2003). Significant changes between CSG03 and the current paper occurred for O I, where  $f(\lambda 1302)$  decreased from 0.052 to 0.048, and Fe II where  $f(\lambda 1144)$  decreased from 0.106 to 0.087,  $f(\lambda 1143)$  increased from 0.0177 to 0.0192, and  $f(\lambda 1122)$  increased from 0.020 to 0.029.

We have gone back to those three sight lines and refitted curves of growth using the new  $f$ -values, recalculated column densities, and calculated abundances relative to the new solar values of AGS05. The wavelengths covered by *HST*-STIS E140M data toward 3C 351 include

TABLE 5  
SUMMARY OF MEASUREMENTS—MRK 290 SIGHTLINE

Species	$\lambda^a$ (Å)	$f^a$	$W_\lambda^b$ (mÅ)	$\log N(X)^b$ ( $N$ in $\text{cm}^{-2}$ )
H I	...	...	...	$20.12^{+0.02}_{-0.02}(\pm 0.1)^c$
N I	1134.415	0.0287	$46 \pm 14$	$14.23^{+0.17}_{-0.20}$
N II	1083.994	0.115	$190 \pm 28$	$14.96^{+1.04}_{-0.48}$
N V	1238.821	0.156	$< 65$	$< 13.49$
O I	929.517	0.00229	$77 \pm 18$	$15.75^{+0.29}_{-0.15}$
...	936.630	0.00365	$105 \pm 17$	...
...	950.885	0.00158	$63 \pm 20$	...
...	971.738	0.0116	$153 \pm 20$	...
...	976.448	0.00331	$69 \pm 19$	...
...	1039.230	0.00907	$142 \pm 10$	...
O VI	1031.926	0.133	$163 \pm 15$	$14.23^{+0.04}_{-0.04}$
Si II	1020.699	0.0168	$83 \pm 12$	$14.93^{+0.18}_{-0.13}$
P II	963.801	1.460	$< 60$	$< 12.82$
S II	1259.518	0.0166	$36 \pm 12$	$14.24^{+0.16}_{-0.20}$
Ar I	1048.220	0.263	$< 32$	$< 13.15$
Mn II	2576.877	0.361	$< 99$	$< 12.74$
Fe II	1121.975	0.0290	$68 \pm 13$	$14.41^{+0.23}_{-0.21}$
...	1144.938	0.0830	$138 \pm 18$	...
...	2344.214	0.114	$361 \pm 36$	...
...	2374.461	0.0313	$199 \pm 48$	...
...	2382.765	0.320	$506 \pm 28$	...
...	2586.650	0.0691	$317 \pm 31$	...
...	2600.173	0.239	$474 \pm 27$	...

<sup>a</sup>Wavelengths and oscillator strengths from Morton (2003).

<sup>b</sup>Equivalent widths for Complex C are integrated over velocity range  $-165$  to  $-75$   $\text{km s}^{-1}$ . Error bars on measured column densities are  $1\sigma$ ; upper limits are  $3\sigma$ . Column densities are calculated from curve of growth with doppler parameter,  $b = 15.7^{+3.6}_{-2.8}$   $\text{km s}^{-1}$ , except for O VI and N V, where we used the AOD method.

<sup>c</sup>The  $N_{\text{HI}}$  column density includes a systematic error (in parentheses) of 0.1 dex, arising from beam-size mismatch between H I 21-cm data and quasar absorption spectra.

only one strong O I line, which does not allow a curve of growth fit. Given the strength of the O I line, unresolved saturation may be an issue. We therefore take the same approach as for PG 1626+554, establishing possible O I column densities for a range of  $b$ -values from  $b = 10.2$  to  $b = 18.0$   $\text{km s}^{-1}$ . Other AOD column densities toward 3C 351 reported in Tripp et al. (2003) are scaled to the new Morton (2003)  $f$ -values, and line upper limits are converted from  $4\sigma$  to  $3\sigma$ . Abundance measurements for all Complex C sight lines are shown in Table 9. Note that the abundances in Table 9 do not include the 0.1 dex systematic error associated with the beam-size mismatch.

#### 4.2. Abundances in Complex C

In order to properly analyze the abundances in Complex C, it is important to include measurements from all available Complex C sight lines. There are four additional Complex C sight lines, not presented here, which have been thoroughly analyzed in previous studies. CSG03 analyzed the additional Complex C sight lines Mrk 817, PG 1259+593, and PG 1351+640. Tripp et al. (2003) included equivalent width and apparent-optical-depth column density measurements toward the 3C 351 sight line.

Using this dataset, we find that Complex C has metallicity ranging from 0.09 to 0.29  $Z_\odot$ , based on the [O I/H I]

abundance. This range is based strictly on the seven Complex C components in six sight lines, where we can empirically fit a curve of growth. Two other sightlines have less reliable values of [O I/H I], owing to a range of possible doppler parameters for the curve of growth. The allowed range of metallicities towards 3C 351 is consistent with the more reliable data, while the range of O I abundances towards PG 1626+554 allows a metallicity as high as 0.39  $Z_\odot$  if  $b = 10.2$   $\text{km s}^{-1}$ . Our reliably measured range,  $Z/Z_\odot = 0.09 - 0.29$ , indicates a factor-of-three variation in metal enrichment across Complex C. The mean O I abundance of those 7 components yields an average Complex C metallicity of 0.17  $Z_\odot$ , with a column-density-weighted mean of 0.13  $Z_\odot$ . As with the conclusions of previous Complex C studies (CSG03; Tripp et al. 2003), these metallicities indicate that Complex C consists of more than just primordial material, with enriched material as well, most likely of Galactic origin (or expelled from Local group dwarfs). As for the range in metallicity, certain regions of Complex C appear to be more highly mixed with enriched gas than others. The  $1\sigma$  errors on these measurements are typically within a factor of 1.5, and the beam-size systematic error is within a factor of 1.25. It is unlikely that these results are consistent with a uniform metallicity for Complex C.

In order to trace possible signatures of gas mixing, we looked for trends in [O I/H I]. One possible signature of gas mixing could be a dependence of [O I/H I] on H I column density. Sight lines passing through low- $N_{\text{HI}}$  regions could trace areas where gas mixing is more efficient, whereas high- $N_{\text{HI}}$  regions mark cloud cores, where mixing may not be as effective. Such a scenario is consistent with the 3 [O I/H I] measurements presented in CSG03. Figure 8 shows a plot of [O I/H I] vs.  $\log N_{\text{HI}}$  for each of the 10 Complex C components presented here. The Mrk 290 measurement encompasses two velocity components. One of the components has much larger  $N_{\text{HI}}$  and dominates the abundance measurement; we therefore consider it as effectively one component. Figure 8 does not include the 0.1 dex systematic error from the beam-size mismatch.

Because of its importance as an indicator of mixing, we now examine Figure 8 for potential metallicity dependence on  $N_{\text{HI}}$ . The two highest column density components, toward PG 1259+593 and Mrk 290, do have the lowest metallicity of  $\sim 10\%$  solar. However, owing to the error bars, the statistical significance of a trend is weak. If we use the column-density weighted mean metallicity (0.13  $Z_\odot$ ), we find a 11% probability that the observed variance in [O I/H I] vs.  $\log N_{\text{HI}}$  occurs purely by chance. Therefore, any slope to the relation of metallicity with  $N_{\text{HI}}$  is present only at the  $2\sigma$  level. In order to properly assess the metallicity dependence on  $N_{\text{HI}}$ , it would be desirable to gain more precise measurements along more sight lines, using additional data from FUSE or from the *Cosmic Origins Spectrograph* scheduled for 2008 installation on HST, in order to reduce the error bars on O I metallicity.

Another possible tracer of gas mixing would be a metallicity dependence on Galactic latitude. Assuming that higher latitude regions of Complex C are at larger distance from the Galactic plane, it is possible that low-latitude sight lines may pierce regions that are closer to

TABLE 6  
SUMMARY OF MEASUREMENTS—MRK 876 SIGHTLINE

Species	$\lambda^a$ (Å)	$f^a$	Component 1		Component 2	
			$W_\lambda^b$ (mÅ)	$\log N(X)^b$ ( $N$ in $\text{cm}^{-2}$ )	$W_\lambda^b$ (mÅ)	$\log N(X)^b$ ( $N$ in $\text{cm}^{-2}$ )
H I	...	...	...	$19.30^{+0.03}_{-0.04}(\pm 0.1)^c$	...	$18.72^{+0.12}_{-0.17}(\pm 0.1)^c$
N I	1199.550	0.132	$96 \pm 13$	$13.90^{+0.12}_{-0.10}$	$< 35$	$< 13.37$
N II	1083.994	0.111	$188 \pm 16$	$14.75^{+0.35}_{-0.22}$	$53 \pm 15$	$13.76^{+0.18}_{-0.19}$
O I	936.630	0.00365	$51 \pm 15$	$15.26^{+0.17}_{-0.14}$	$< 40$	$14.79^{+0.18}_{-0.11}$
...	948.686	0.00631	...	...	$35 \pm 11$	...
...	971.738	0.0116	...	...	$56 \pm 12$	...
...	976.448	0.00331	$56 \pm 15$	...	$< 38$	...
...	1039.230	0.00907	$92 \pm 10$	...	...	...
...	1302.169	0.0480	$253 \pm 7$	...	$169 \pm 6$	...
Al II	1670.787	1.740	$301 \pm 16$	$13.43^{+0.31}_{-0.19}$	$103 \pm 15$	$12.51^{+0.13}_{-0.11}$
Si II	1020.699	0.0168	$42 \pm 5$	$14.56^{+0.11}_{-0.09}$	$< 14$	$13.85^{+0.09}_{-0.09}$
...	1190.416	0.292	$245 \pm 9$	...	$140 \pm 8$	...
...	1193.290	0.582	$251 \pm 10$	...	$173 \pm 8$	...
...	1304.370	0.0863	$202 \pm 7$	...	$69 \pm 7$	...
...	1526.707	0.133	$261 \pm 10$	...	$116 \pm 9$	...
S II	1253.805	0.0109	$< 31$	$< 14.34$	$< 26$	$< 14.26$
Ar I	1048.220	0.263	$< 15$	$< 12.79$	$< 16$	$< 12.83$
Fe II	1063.176	0.0547	...	$14.36^{+0.07}_{-0.07}$	$23 \pm 5$	$13.72^{+0.15}_{-0.13}$
...	1121.975	0.0290	$49 \pm 5$	...	$< 12$	...
...	1125.448	0.0156	$37 \pm 5$	...	$< 12$	...
...	1143.226	0.0192	$39 \pm 5$	...	$< 14$	...
...	1144.938	0.0830	$131 \pm 5$	...	$41 \pm 5$	...
...	1608.451	0.0577	$187 \pm 17$	...	$72 \pm 15$	...

<sup>a</sup>Wavelengths and oscillator strengths from Morton (2003).

<sup>b</sup>Equivalent widths for Complex C are integrated over velocity range  $-155$  to  $-85$   $\text{km s}^{-1}$  for Component 1 and  $-210$  to  $-155$   $\text{km s}^{-1}$  for Component 2. Error bars on measured column densities are  $1\sigma$ ; upper limits are  $3\sigma$ . Column densities are calculated from curves of growth with doppler parameters,  $b = 17.8^{+2.0}_{-1.8}$   $\text{km s}^{-1}$  for Component 1 and  $b = 15.4^{+3.5}_{-2.5}$   $\text{km s}^{-1}$  for Component 2, except for O VI and N V, where we used the AOD method.

<sup>c</sup>The  $N_{\text{HI}}$  column density includes a systematic error (in parentheses) of 0.1 dex, arising from beam-size mismatch between H I 21-cm data and quasar absorption spectra.

TABLE 7  
COMPLEX C HIGHLY IONIZED COMPONENT—MRK 876 SIGHTLINE<sup>a</sup>

Species	$\lambda^a$ (Å)	$f^b$	$W_\lambda^b$ (mÅ)	$\log N(X)^c$ ( $N$ in $\text{cm}^{-2}$ )
C IV	1548.204	0.190	$199 \pm 19$	$13.80^{+0.04}_{-0.03}$
...	1550.781	0.0948	$96 \pm 20$	$13.81^{+0.06}_{-0.08}$
Si IV	1393.760	0.513	$134 \pm 9$	$13.28^{+0.03}_{-0.02}$
...	1402.773	0.254	$41 \pm 9$	$13.01^{+0.09}_{-0.10}$
N V	1238.821	0.156	$< 43$	$< 13.32$
O VI	1031.926	0.133	$153 \pm 9$	$14.20^{+0.02}_{-0.02}$

<sup>a</sup>Data for the high ions are presented separately since they have a distinctly different velocity range and profile than the low ions presented in Table 4.

<sup>b</sup>Wavelengths and oscillator strengths from Morton (2003). Equivalent widths of the highly ionized component are measured over velocity range  $-210$  to  $-75$   $\text{km s}^{-1}$ .

<sup>c</sup>Error bars on measured column densities are  $1\sigma$ ; upper limits are  $3\sigma$ . Column densities are measured with the AOD method.

TABLE 8  
SUMMARY OF MEASUREMENTS—PG 1626+554 SIGHTLINE

Species	$\lambda^a$ (Å)	$f^a$	$W_\lambda^b$ (mÅ)	$\log N(X)^b$ ( $N$ in $\text{cm}^{-2}$ )
H I	...	...	...	$19.43^{+0.02}_{-0.02}(\pm 0.1)^c$
N I	1134.165	0.0146	$< 50$	$< 14.49$
O I	1039.230	0.00907	$107 \pm 12$	$[15.30^{+0.08}_{-0.08}, 15.68^{+0.22}_{-0.19}]$
O VI	1031.926	0.133	$119 \pm 16$	$14.10^{+0.05}_{-0.06}$
Si II	1020.699	0.0168	$46 \pm 15$	$14.56^{+0.11}_{-0.16}$
Ar I	1048.220	0.263	$< 44$	$< 13.25$
Fe II	1144.938	0.0830	$102 \pm 16$	$[14.19^{+0.10}_{-0.11}, 14.45^{+0.22}_{-0.19}]$

<sup>a</sup>Wavelengths and oscillator strengths from Morton (2003).

<sup>b</sup>Equivalent widths for Complex C are integrated over velocity range  $-155$  to  $-75$   $\text{km s}^{-1}$ . Error bars on measured column densities are  $1\sigma$ ; upper limits are  $3\sigma$ . Ranges of column densities for O I and Fe II are calculated from curves of growth with doppler parameters,  $b = 10.2$   $\text{km s}^{-1}$  and  $b = 18.0$   $\text{km s}^{-1}$  (in brackets). The AOD method is used for all other species.

<sup>c</sup>The  $N_{\text{HI}}$  column density includes a systematic error (in parentheses) of 0.1 dex because of beam-size mismatch between H I 21-cm data and quasar absorption spectra.

the disk and more highly enriched by solar-metallicity fountain material. Referring to a sight-line map of Complex C (e.g., Figure 1 of CSG03), such a scenario is not

borne out by the data. Although the two lowest metallic sight lines are at relatively high latitude, the highest-

TABLE 9  
COMPLEX C ABUNDANCE MEASUREMENTS<sup>a</sup>

Sight Line	$\log N_{\text{HI}} \text{ (cm}^{-2}\text{)}$	O I	N I	Si II	Fe II	S II	Ar I
3C 351 <sup>b</sup>	$18.62^{+0.03}_{-0.03}$	$[-0.91^{+0.06}_{-0.07}, -0.67^{+0.08}_{-0.08}]$	$<-1.08$	$-0.35^{+0.12}_{-0.12}$	$-0.29^{+0.08}_{-0.10}$	$< 0.12$	...
HS 1543+5921 <sup>b</sup>	$19.67^{+0.05}_{-0.07}$	...	$[-1.22^{+0.17}_{-0.17}, -0.53^{+0.50}_{-0.43}]$	...	...	$-0.51^{+0.10}_{-0.12}$	...
Mrk 205	$18.11^{+0.09}_{-0.11}$	$-0.78^{+0.12}_{-0.13}$	$<-0.63$	$-0.51^{+0.16}_{-0.15}$	$<-0.13$	$< 0.57$	$< 0.60$
Mrk 279	$19.27^{+0.08}_{-0.11}$	$-0.95^{+0.14}_{-0.13}$	$-1.83^{+0.14}_{-0.17}$	$-0.64^{+0.11}_{-0.14}$	$-0.87^{+0.14}_{-0.16}$	$-0.72^{+0.14}_{-0.19}$	$<-0.76$
Mrk 290	$20.12^{+0.02}_{-0.02}$	$-1.03^{+0.29}_{-0.16}$	$-1.67^{+0.18}_{-0.21}$	$-0.70^{+0.19}_{-0.14}$	$-1.16^{+0.24}_{-0.22}$	$-1.02^{+0.17}_{-0.21}$	$<-1.15$
Mrk 817	$19.51^{+0.01}_{-0.01}$	$-0.54^{+0.16}_{-0.09}$	$<-1.17$	$-0.56^{+0.09}_{-0.09}$	$-0.68^{+0.08}_{-0.09}$	$-0.31^{+0.09}_{-0.08}$	$<-1.03$
Mrk 876- C. 1	$19.30^{+0.03}_{-0.04}$	$-0.70^{+0.18}_{-0.15}$	$-1.18^{+0.14}_{-0.12}$	$-0.25^{+0.12}_{-0.11}$	$-0.39^{+0.09}_{-0.09}$	$<-0.10$	$<-0.69$
Mrk 876- C. 2	$18.72^{+0.12}_{-0.17}$	$-0.59^{+0.22}_{-0.21}$	$<-1.13$	$-0.38^{+0.16}_{-0.20}$	$-0.45^{+0.20}_{-0.22}$	$< 0.40$	$<-0.07$
PG 1259+593	$19.95^{+0.01}_{-0.01}$	$-1.00^{+0.21}_{-0.18}$	$-1.81^{+0.25}_{-0.18}$	$-0.80^{+0.22}_{-0.18}$	$-1.01^{+0.12}_{-0.11}$	$-0.71^{+0.10}_{-0.10}$	$-1.05^{+0.12}_{-0.14}$
PG 1351+640	$19.83^{+0.02}_{-0.02}$	$<-0.42$	$<-0.75$	$-0.44^{+0.31}_{-0.20}$	$-0.50^{+0.26}_{-0.18}$	$<-0.47$	$<-0.60$
PG 1626+554 <sup>b</sup>	$19.43^{+0.02}_{-0.02}$	$[-0.79^{+0.10}_{-0.10}, -0.41^{+0.23}_{-0.20}]$	$<-0.72$	$-0.38^{+0.12}_{-0.17}$	$[-0.69^{+0.11}_{-0.12}, -0.43^{+0.23}_{-0.20}]$	...	$<-0.36$

<sup>a</sup>The abundance of element X is calculated relative to H I. The 0.1 dex systematic error due to the beam-size mismatch between H I 21-cm data and the quasar absorption spectra is not listed.

<sup>b</sup>Column density range for quantities in brackets is calculated assuming doppler parameter  $10.2 < b < 18.0 \text{ km s}^{-1}$ .

metallicity sight line, toward Mrk 817, is also at high latitude. Although, the magnitude and variation in sight-line metallicity indicates different degrees of primordial and enriched gas mixing throughout Complex C, the signature of mixing versus Galactic latitude is not apparent.

#### 4.3. Relative Abundances and Nucleosynthetic History

An additional issue worth consideration is the nucleosynthetic history of the cloud as revealed by relative abundance patterns. Previous Complex C studies have found evidence of  $\alpha$ -element (S, Si, O) enhancement and nitrogen depletion, indicating that Complex C has been enriched primarily by metals produced by Type II SNe (Richter et al. 2001; CSG03; Tripp et al. 2003). These topics can be investigated more fully, now that column densities of O I and N I have been measured for several more sight lines. The consideration of relative abundances instead of absolute abundances has the additional advantage that the problem of UV/radio beam-size mismatch is not applicable. In order to consider relative abundances, we have calculated the column-density-weighted abundances of S II, Si II, Fe II, and N I, relative to O I. We only include a sight line's relative abundance if abundances of both of the considered ion species have been measured. These totals are:  $[\text{S II/O I}] = 0.16^{+0.16}_{-0.13}$ ,  $[\text{Si II/O I}] = 0.27^{+0.19}_{-0.13}$ ,  $[\text{Fe II/O I}] = -0.03^{+0.16}_{-0.12}$ , and  $[\text{N I/O I}] = -0.69^{+0.21}_{-0.17}$ . The  $[\text{N I/O I}]$  ratio is based on only the four sight lines in which N I lines were successfully measured. The cases with only upper limits are also consistent with a significantly depleted N I relative abundance. Toward Mrk 817 and in Component 2 toward Mrk 876, we find Complex C abundances of  $[\text{N I/O I}] < -0.63$  and  $[\text{N I/O I}] < -0.54$ , respectively.

In order to determine relative elemental abundances from ion abundances, one must make ionization corrections, defined for example as  $[\text{S/H}] = [\text{S II/H I}] + (\text{correction})$ , where logarithmic quantities are implied. Such corrections are uncertain, because they depend on the

gas density and ionizing radiation field. CSG03 calculated such corrections, using the photoionization code Cloudy (Ferland et al. 1998; see Figure 16 from CSG03). The corrections were negligible for O I and N I, which are coupled to H I through charge exchange. Using version 06.02 of Cloudy, we have updated these calculations, constructing a new grid of models with input parameters similar to those described in CSG03, but with relative abundances consistent with AGS05. The results for O I and N I, as well as Si II, S II, and Fe II are similar to that shown in CSG03 for  $\log N_{\text{HI}}$  down to 19. The new sightline, toward MRK 205, for which  $\log N_{\text{HI}} = 18.1$ , will have larger ionization corrections but the limited data available here will not impact our column density weighted results. The doubly ionized species, Si II, S II, and Fe II, occur in both H I and H II regions, and ionization corrections are necessary to properly compare relative abundances involving these singly-ionized species. For Si, S, and Fe, the sign of the correction is negative (abundances of Si, S, and Fe are *less* than inferred from Si II/H I, S II/H I, Fe II/H I) and the magnitude decreases at larger  $N_{\text{HI}}$ . Because the mean relative abundances are weighted by column density, the ionization correction is fairly small for S II, Si II, and Fe II, ranging from 0.1–0.2 dex, with Fe II requiring roughly half the logarithmic correction as Si II and S II.

Considering a rough ionization correction to the above relative ion abundances, the  $\alpha$ -elements (S, Si, and O) have an essentially solar pattern and are slightly enhanced relative to Fe. Nitrogen is depleted by a factor of 5 from a solar relative abundance pattern. The enrichment of  $\alpha$ -elements relative to N and Fe suggests that the metals were produced primarily by massive stars and injected into the ISM by Type II SNe. Nitrogen and iron are typically produced in longer-lived stars, so an  $\alpha$ -enhancement is a signature of gas that has been stripped quickly from the star-forming region. Material ejected from the disk by vigorous SN activity in a Galactic fountain, or falling into the disk from galactic winds in Local

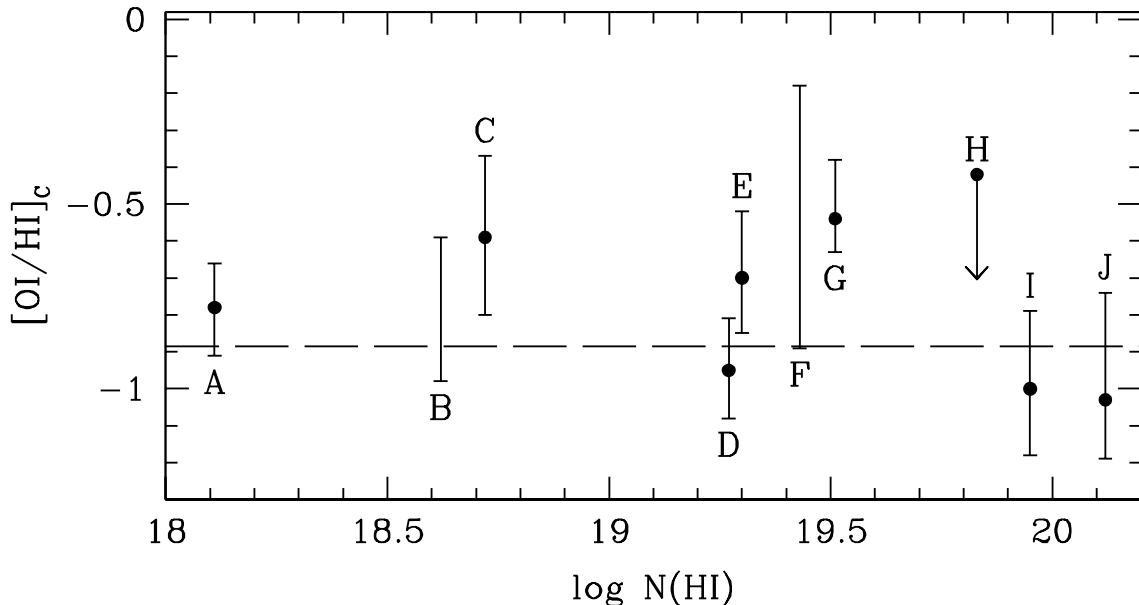


FIG. 8.— Plots of  $[O\ I/H\ I]$  vs. H I column density for the 9 Complex-C sight lines (10 velocity components) discussed in this paper. Seven components have reliably measured  $[O\ I/H\ I]$ . Dotted line shows the column density weighted mean of  $0.13Z_{\odot}$ .  $[O\ I/H\ I]$  measurements towards 3C 351 and PG 1626+554 are illustrated by a range that includes the  $1\sigma$  error bars on the minimum and maximum values arising from the uncertain range in  $b$ . Letters next to data points identify the Complex C components as follows: A) Mrk 205; B) 3C 351; C) Mrk 876, Component 2; D) Mrk 279; E) Mrk 876, Component 1; F) PG 1626+554; G) Mrk 817; H) PG 1351+640; I) PG 1259+593; J) Mrk 290.

Group dwarf galaxies, is consistent with such a scenario. A plausible explanation, then, for the observed metallicity and abundance pattern is that Complex C is mixing with wind/fountain material as it falls onto the Milky Way disk.

We now have a fairly complete set of Ar I upper limits and one reliable Ar I detection. Table 9 shows the Ar I abundance results for each Complex C component. We have only one reliable Complex C detection, toward PG 1259+593 (CSG03; Sembach et al. 2004), where  $[Ar\ I/H\ I] = -1.05^{+0.15}_{-0.14}$  (9% solar) with  $\log N_{HI} = 19.95$  relative to an assumed solar abundance  $(Ar/H)_{\odot} = 1.5 \times 10^{-6}$ . Many of the other Complex C sight lines have lower  $N_{HI}$ , insufficient to detect the weak Ar I lines at 1048 and 1066 Å without extremely long exposures (PG 1259+593 had total exposure  $\sim 600$  ks). However, we should have been able to detect Ar I toward Mrk 290, with  $\log N_{HI} = 20.12$ , but we only measured an upper limit,  $\log N(Ar\ I) < 13.15$ , corresponding to  $[Ar\ I/H\ I] < -1.15$  (7% solar).

Such low values for  $[Ar\ I/H\ I]$  are not entirely due to metallicity, as argon probably has a substantial (positive) ionization correction. This effect is similar to that seen (Jenkins et al. 2000) in the local ISM toward four white dwarfs, where they found that Ar I is deficient by 0.4 dex, probably because Ar I is more easily ionized than H I. This effect probably arises (Sofia & Jenkins 1998) because Ar I has a large photoionization cross section near threshold (15.755 eV) that enhances the abundance in the Ar II ionization stage. From our grid of photoionization models, we find that a positive ionization correction is likely appropriate. For  $\log N_{HI} = 20$ , this correction may range from 0.1 dex to as much as 0.4 dex if the volume density is as low as  $0.01\text{ cm}^{-3}$ .

#### 4.4. High Ions in Complex C

In addition to allowing a thorough investigation of the ion abundance pattern in Complex C, these new data provide the spectral coverage to analyze highly-ionized species. The most useful way to study the high ions is through the comparison of high-ion ratios involving C IV, Si IV, N V, and O VI. In order to carry out such an analysis, we require that Complex C sight lines have both STIS E140M and *FUSE* data. Until the acquisition of the new data presented in this paper, the only sight line with both *FUSE* and STIS E140M data was PG 1259+593. F04 thoroughly investigated the high-ions in Complex C toward PG 1259+593 and found that the values are consistent with the high ions arising through collisional ionization at the interface of Complex C and a surrounding hotter medium. With the new STIS E140M data for Mrk 279 and Mrk 876, we can now investigate Complex C high ions in three sight lines.

Table 10 shows the logarithmic column density ratios involving C IV, Si IV, N V, and O VI for these three sight lines. Included is the PG 1259+593 measurement from CSG04. The high ion absorption lines are typically weak and show little evidence of saturation. The  $W_{\lambda}$  measurements of the C IV and Si IV doublets toward Mrk 876 confirm an absence of saturation. In the cases of Mrk 279 and PG 1259+593, the weaker lines of the C IV and Si IV doublets cannot be measured. Owing to their lack of saturation and better detectability, we use the stronger lines of these doublets to calculate column density ratios. The high-ion ratios are remarkably similar for each of the three sight lines. Although N V cannot be measured, the values for  $[C\ IV/O\ VI]$  and  $[Si\ IV/O\ VI]$  vary by no more than 0.1 dex.

These measured ratios can be compared to ionization

TABLE 10  
COMPLEX C LOGARITHMIC COLUMN DENSITY  
RATIOS<sup>a</sup>

Sight Line	[C IV/O VI]	[Si IV/O VI]	[N V/O VI]
Mrk 279	$-0.36^{+0.06}_{-0.06}$	$-0.93^{+0.06}_{-0.06}$	$< -0.82$
Mrk 876	$-0.40^{+0.04}_{-0.04}$	$-0.92^{+0.04}_{-0.04}$	$< -0.88$
PG 1259+593	$-0.31^{+0.03}_{-0.09}$	$-0.90^{+0.11}_{-0.14}$	$< -0.38$

<sup>a</sup>We present high-ion ratios for only these three sightlines for which *FUSE* and *HST* data provide wavelength coverage of the UV lines for O VI (1032 Å), C IV (1548 Å), N V (1238 Å), and Si IV (1394 Å).

models. Photoionization models used to fit high ions in HVCs require a large ionization parameter, and thus low gas density and size  $\sim 100$  kpc (F04, CSG04). With an approximate upper limit on the distance to Complex C at  $\lesssim 25$  kpc (Wakker et al. 1999) and, in turn, a size no larger than a few kpc, photoionization can be ruled out for producing the high ions in Complex C. Collisional ionization can produce copious amounts of high ions, while photoionization with a more reasonable ionization parameter can produce the low ions. F04 consider several common collisional ionization models for the case of a low-metallicity cloud. They present corrected high-ion ratio predictions for these models, using C, O, Si, and N abundances appropriate for Complex C. The abundances they use are based on the PG 1259+593 results, which differ from what we measure towards Mrk 279 and Mrk 876, and from the PG 1259+593 results presented here, although they agree to within 0.2 dex. This uncertainty in the input to the corrected models is small compared to the predicted ranges of high-ion ratios, and thus does not significantly affect the analysis.

Comparing the high-ion measurements to the corrected models of F04, we can assess possible ionization sources. We find that the observed high ion ratios can be explained by subsolar abundance models of shock ionization (Dopita & Sutherland 1996) or turbulent mixing layers (Slavin, Shull, & Begelman 1993). The conductive interface model (Borkowski, Balbus, & Fristrom 1990) produces lower ratios of [Si IV/O VI] than observed. However Si III is more easily photoionized (ionization potential = 33.5 eV) than the other high ions. If the bulk of the Si IV is produced through photoionization, then ionization on conductive interfaces could explain the production of the other high ions. Although one can relax the size requirements on collisionally ionized high ions, one still cannot violate the mass constraints (CSG05) of placing the system of HVC O VI at large distances (100 kpc to Mpc scales).

Although one cannot prove that high-velocity O VI is co-spatial with the low ions, its kinematic association suggests a connection. In our previous papers (CSG04, CSG05), we discussed hybrid ionization models, in which high- and low-ions are produced by a combination of photoionization and collisional ionization, as in bow shocks and other interfaces. Collisional ionization by extended ( $D > 100$  kpc) low-density gas requires too much mass and is inconsistent with halo scale lengths. Each of the viable collisional ionization sources requires interaction

between Complex C and a surrounding environment. For turbulent mixing and conductive heating, the interaction is from immersion in a surrounding hotter medium, possibly an extended Galactic corona. Shock ionization may occur in a bowshock as the Complex plunges through the halo towards the disk. The shock possibility was explored (CSG04, CSG05) as a method of producing the high ions in highly ionized HVCs. The line profile kinematics support the scenario of the high ions tracing the outer envelope or leading edge of Complex C. High-ions often extend over a larger velocity range than the low ions, suggesting that the low ions trace denser, photoionized gas at the cloud core. Such an effect is seen in the data for Mrk 279, Mrk 290, and PG 1626+554.

The remarkable kinematics of the high ions toward Mrk 876 suggest a decelerated bowshock, since the high-velocity C IV and Si IV profiles peak at  $+30$  km s<sup>-1</sup> from the low ions. Further, the high ions are well blended with lower velocity gas, whereas the low ions are not, suggesting a possible mixing of hot gas in Complex C and the Galactic halo. The high ions toward Mrk 876 may trace a decelerating shocked medium at the leading edge of the cloud as it falls through and interacts with the Galactic halo.

Analysis of the high ions in Complex C can also be used to understand the nature of the highly ionized HVCs by comparing to the high ion ratios (C IV, Si IV, N V, O VI) presented by CSG05. Although they show a larger spread, the high-ion ratios for the highly ionized HVCs that are detected in singly-ionized species are similar to the values presented in Table 11, suggesting a similar ionization source. Only the highly ionized HVCs detected in O VI alone show a marked deviation from what is observed in Complex C sight lines. The characterization of the Complex C high ions in this work adds further to the proposal by CSG05 that the majority of highly ionized HVCs represent low- $N_{\text{HI}}$  analogs to the large HVCs like Complex C.

## 5. CONCLUSIONS

In this paper, we assembled the latest dataset of *FUSE* and *HST*-STIS spectra of 10 Complex C sight lines. Including new data for several sightlines, and reanalyzing previous data, we derived abundance ratios for 11 Complex C velocity components detected in UV absorption lines. We also revised or updated the H I (21-cm) column densities, solar abundances, and absorption oscillator strengths. Values of  $\log N_{\text{HI}}$  from 21-cm emission typically changed by  $\leq 0.03$  between our 2003 analysis, based on Wakker et al. (2001), and our current analysis, based on Wakker et al. (2003).

Using the new data, with revised values of  $N_{\text{HI}}$ , solar abundances, and absorption-line  $f$ -values, we arrive at the following conclusions:

1. *Metallicity.* We measure the ratio of [O I/H I] with curve-of-growth techniques in seven Complex C components and constrain the ratio in two other components. The O I abundance has been argued to be an accurate tracer of gas metallicity based on charge-exchange coupling with H I. Our results significantly improve the statistics of Complex C metallicity measurements from previous studies. Based on [O I/H I], we find that the metallicity



of Complex C varies from 0.09 to 0.29  $Z_{\odot}$ . This factor-of-three variance in metallicity is unlikely to be attributed to systematic uncertainties such as mismatched radio-emission and UV-absorption beam sizes. The column-density weighted mean metallicity of the sample is  $Z = 0.13 Z_{\odot}$ , with a possible but unconfirmed ( $2\sigma$ ) correlation of lower metallicity along sightlines with higher  $N_{\text{HI}}$ . However, with our current data, the variations in metallicity and their error bars make it difficult to prove this trend. Better data might demonstrate more efficient mixing of infalling gas with lower- $N_{\text{HI}}$  gas in the Complex-C envelopes, compared to lower-metallicity cloud cores.

2. *Relative Abundances.* The abundance ratio [N I/H I] indicates a significant  $\alpha$ -element enrichment in Complex C gas. We measure [N I/H I] over the range 0.01 to 0.07 (N/H) $_{\odot}$  in four sight lines. Comparing to the O I abundance, we measure a column density weighted mean relative abundance of 0.20 (N/O) $_{\odot}$ . Further, Fe is slightly depleted relative to the  $\alpha$ -elements (O, S, Si). The enrichment of  $\alpha$ -elements relative to N and Fe suggests metal production by massive stars, with subsequent contamination of the ISM by Type II SNe (gas in the Galactic fountain or expelled from Local Group dwarfs). Such a nucleosynthetic history is consistent with Complex C metal enrichment by fountain or wind material, as the object interacts

with the Galactic halo.

3. *Highly Ionized Gas.* The three sight lines with both *FUSE* and *HST-STIS* data allow spectral coverage of the key high ions C IV, Si IV, N V, and O VI. The high ion column density ratios are nearly identical for each of three sight lines, and are consistent with the presence of hot  $10^5 - 10^6$  K gas at the cloud interface. The highly ionized ratios are adequately explained by either ionization by shocks or an interaction with a surrounding medium via turbulent mixing or conductive interfaces. The high ion ratios of the H I-detected Complex C are similar to those of the highly ionized HVCs, which are detected only in UV absorption spectra. The possible similarity in ionization mechanism suggests each of these classes of HVCs may trace the same phenomenon, though at different ends of the HVC column density distribution.

We acknowledge support from NASA/FUSE grant NNG04GO36G and STScI archival grant AR-10645.02-A at the University of Colorado. The FUSE data were obtained by the Guaranteed Time Team for the NASA-CNES-CSA mission operated by the Johns Hopkins University. Financial support to U.S. participants was provided by NASA contract NAS5-32985.

#### REFERENCES

- Anders, E., & Grevesse, N. 1989, *Geochim. Cosmochim. Acta*, 53, 197
- Asplund, M., Grevesse, N., & Sauval, A. J. 2005, in ASP Conf. Ser. 336, *Cosmic Abundances as Records of Stellar Evolution and Nucleosynthesis*, eds. T. G. Barnes III and F. N. Bash (San Francisco: ASP), 25 (AGS05)
- Ayres, T. R., Plymate, C., & Keller, C. U. 2006, *ApJS*, 165, 618
- Bahcall, J. N., Basu, S., Pinsonneault, M., & Serenelli, A. M. 2005, *ApJ*, 618, 1049
- Bland-Hawthorn, J., & Putman, M. E. 2001, in ASP Conf. Ser. 240, *Gas and Galaxy Evolution*, eds. J. E. Hibbard, M. Rupen, and J. H. van Gorkom (San Francisco: ASP), 369
- Borkowski, K. J., Balbus, S. A., & Fristrom, C. C. 1990, *ApJ*, 355, 501
- Bowen, D. V., Jenkins, E. B., Pettini, M., & Tripp, T. M. 2005, *ApJ*, 635, 880
- Bregman, J. N. 1980, *ApJ*, 236, 577
- Collins, J. A., Shull, J. M., & Giroux, M. L. 2003, *ApJ*, 585, 336 (CSG03)
- Collins, J. A., Shull, J. M., & Giroux, M. L. 2004, *ApJ*, 605, 216 (CSG04)
- Collins, J. A., Shull, J. M., & Giroux, M. L. 2005, *ApJ*, 623, 196 (CSG05)
- Dopita, M. A., & Sutherland, R. S. 1996, *ApJS*, 102, 161
- Ferland, G. J., Korista, K. T., Verner, D. A., Ferguson, J. W., Kingdon, J. B., & Verner, E. M. 1998, *PASP*, 110, 761
- Fox, A. J., Savage, B. D., Wakker, B. P., Richter, P., Sembach, K. R., & Tripp, T. M. 2004, *ApJ*, 602, 737 (F04)
- Gibson, B. K., Giroux, M. L., Penton, S. V., Stocke, J. T., Shull, J. M., & Tumlinson, J. 2001, *AJ*, 122, 3280
- Gillmon, K., Shull, J. M., Tumlinson, J., & Danforth, C. 2006, *ApJ*, 636, 891
- Grevesse, N., & Sauval, A. J. 1998, *SSRv*, 85, 161
- Hartmann, D., & Burton, W. B. 1997, *Atlas of Galactic Neutral Hydrogen* (Cambridge: Cambridge Univ. Press)
- Henry, R. B. C., Edmunds, M. G., Köppen, J. 2000, *ApJ*, 541, 660
- Jenkins, E. B., et al. 2000, *ApJ*, 538, L81
- Moos, H. W., et al. 2000, *ApJ*, 538, L1
- Morton, D. C., 2003, *ApJS*, 149, 205
- Murphy, E. M., et al. 2000, *ApJ*, 538, L35
- Nicastro, F., et al. 2002, *ApJ*, 573, 157
- Nicastro, F., et al. 2003, *Nature*, 421, 719
- Pagel, B. E. J. 1994, in *The Formation and Evolution of Galaxies*, ed. C. Munez-Tunón & F. Sánchez (Cambridge: Cambridge Univ. Press), 149
- Pettini, M. 2004, in *Cosmochemistry: The Melting Pot of Elements*, eds. C. Esteban et al. (Cambridge: Cambridge Univ. Press), 257
- Richter, P., et al. 2001, *ApJ*, 559, 318
- Sahnow, D. J., et al. 2000, *ApJ*, 538, L7
- Savage, B. D., & Sembach, K. R. 1991, *ApJ*, 379, 245
- Sembach, K. R., Savage, B. D., Lu, L., & Murphy, E. M. 1999, *ApJ*, 515, 108
- Sembach, K. R., et al. 2003, *ApJS*, 146, 165
- Sembach, K. R., et al. 2004, *ApJS*, 150, 387
- Shapiro, P. R., & Field, G. B. 1976, *ApJ*, 205, 762
- Slavin, J. D., Shull, J. M., & Begelman, M. C. 1993, *ApJ*, 407, 83
- Sofia, U. J., & Jenkins, E. B. 1998, *ApJ*, 499, 951
- Tripp, T. M., et al. 2003, *AJ*, 125, 3122
- Wakker, B. P. 2001, *ApJS*, 136, 463
- Wakker, B. P., et al. 1999, *Nature*, 402, 388
- Wakker, B. P., et al. 2003, *ApJS*, 146, 1
- Wakker, B. P., Kalberla, P. M. W., van Woerden, H., de Boer, K. S., & Putman, M. E. 2001, *ApJS*, 136, 537
- Wakker, B. P., & van Woerden, H. 1997, *ARA&A*, 35, 217